

Pilot-wave dynamics in a rotating frame: the onset of orbital instability

Nicholas Liu¹, Matthew Durey² and John W.M. Bush¹,†

(Received 1 June 2023; revised 31 July 2023; accepted 1 September 2023)

We report the results of a theoretical investigation of the stability of a hydrodynamic analogue of Landau levels, specifically circular orbits arising when a millimetric droplet self-propels along the surface of a vibrating, rotating liquid bath. Our study elucidates the form of the stability diagram characterising the critical memory at which circular orbits destabilise, and the form of instability. Particular attention is given to rationalising observations reported in prior experimental works, including the prevalence of resonant wobbling instabilities, in which the instability frequency is approximately twice the orbital frequency. We also explore the physical mechanism responsible for the onset of instability. Specifically, we compare the efficacy of different heuristic arguments proposed in prior studies, including propositions that the most unstable orbits arise when their radii correspond to the zeros of Bessel functions or when their associated wave intensity is extremised. We establish a new relation between orbital stability and the mean wave field, which supersedes existing heuristic arguments and suggests a rationale for the alternate wobbling and monotonic instabilities arising at onset as the orbital radius is increased progressively.

Key words: Faraday waves, drops

1. Introduction

Millimetric droplets may bounce and self-propel along the surface of a vertically vibrating liquid bath (Couder *et al.* 2005*a,b*). These walking droplets, or 'walkers', provide a tangible macroscopic example of wave–particle duality and represent a classical realisation of a pilot-wave system of the form envisaged by de Broglie (1926, 1930) in the 1920s. Since its discovery in 2005, the hydrodynamic pilot-wave system has provided the basis for an unexpectedly long list of hydrodynamic quantum analogues (Bush 2015; Bush & Oza 2020). Notable examples include single-particle diffraction and interference (Couder

† Email address for correspondence: bush@math.mit.edu

¹Department of Mathematics, Massachusetts Institute of Technology, Cambridge, MA 02139, USA

²School of Mathematics and Statistics, University of Glasgow, University Place, Glasgow G12 8QQ, UK

& Fort 2006; Pucci *et al.* 2018; Ellegaard & Levinsen 2020), unpredictable tunnelling (Eddi *et al.* 2009; Tadrist *et al.* 2020), Friedel oscillations (Sáenz, Cristea-Platon & Bush 2020), spin lattices (Sáenz *et al.* 2021), and quantum-like statistics in corrals (Harris *et al.* 2013; Sáenz, Cristea-Platon & Bush 2018). Of particular interest here are the quantised orbits emerging when a droplet walks in the presence of an imposed force (Fort *et al.* 2010; Perrard *et al.* 2014b).

Faraday waves are generated at the free surface of a vibrating liquid bath when the bath's vibrational acceleration exceeds a critical value known as the Faraday threshold (Benjamin & Ursell 1954; Miles & Henderson 1990). Walking droplets arise just below this threshold, and so respond only to the waves generated by their own bouncing. A key feature of the walker system is that the droplets bounce at the frequency of the bath's most unstable Faraday waves, specifically half the frequency of the bath's vibrational forcing. The resulting resonance between the bouncing droplet and the bath ensures that the pilot-wave field is quasi-monochromatic, with a dominant wavelength prescribed by the Faraday wavelength. The dynamics is local in that the droplet responds to the local slope of its guiding wave; however, as the slope is determined by the droplet's past trajectory, the droplet dynamics are non-Markovian. The path memory of the system determines the mean number of prior impacts that contribute to the wave force acting on the droplet, and is prescribed by the proximity of the vibrational acceleration to the Faraday threshold (Eddi et al. 2011). The quantum features of the pilot-wave hydrodynamic system emerge in the high-memory limit arising when the vibrational acceleration approaches the Faraday threshold, and the pilot wave is most persistent.

Orbital quantisation is a canonical feature of the hydrodynamic pilot-wave system, and one of its most compelling as a quantum analogue. At sufficiently high memory, the quasi-monochromatic form of the guiding or 'pilot' wave constrains the droplet to quantised dynamical states (Fort et al. 2010; Oza et al. 2014a; Perrard et al. 2014b; Labousse et al. 2016a). Orbital quantisation has been shown to arise for walkers in a rotating frame (Fort et al. 2010; Harris & Bush 2014; Oza et al. 2014a), a simple harmonic potential (Perrard et al. 2014a,b; Labousse et al. 2016a; Durey & Milewski 2017), and confinement to a submerged well (Harris et al. 2013; Cristea-Platon, Sáenz & Bush 2018; Durey, Milewski & Wang 2020a). In the first of these systems, quantised states consist of circular orbits (Fort et al. 2010). In the latter two systems, more complex orbits may arise, including lemniscates and trefoils (Cristea-Platon et al. 2018; Durey et al. 2020a), and orbits are quantised in both energy and angular momentum (Perrard et al. 2014b). In all three systems, in the high-memory limit the quantised orbits destabilise, and the droplet switches intermittently between the accessible orbits, giving rise to statistics reminiscent of their quantum counterpart (Harris et al. 2013; Oza et al. 2014a,b; Labousse et al. 2016a; Cristea-Platon *et al.* 2018).

The first investigation of droplets walking in a rotating frame was that of Fort *et al.* (2010), who observed that the droplets move in circular orbits (see figure 1). At lower path memory, the orbital radius depends continuously on the bath rotation rate in a manner expected to arise for inertial orbits, from a balance between centripetal and Coriolis forces. At higher memory, the geometric constraint imposed by the monochromatic Faraday wave field restricts the permissible stable orbital radii, giving rise to an effective quantisation in orbital radii. The authors noted that the Coriolis force takes the same form as the Lorentz force on a moving charged particle, and so drew the analogy between the quantised inertial orbits arising in their system and the Landau levels arising when a charged quantum particle moves in a uniform magnetic field. The observed orbital quantisation was captured in their accompanying simulations (Fort *et al.* 2010).

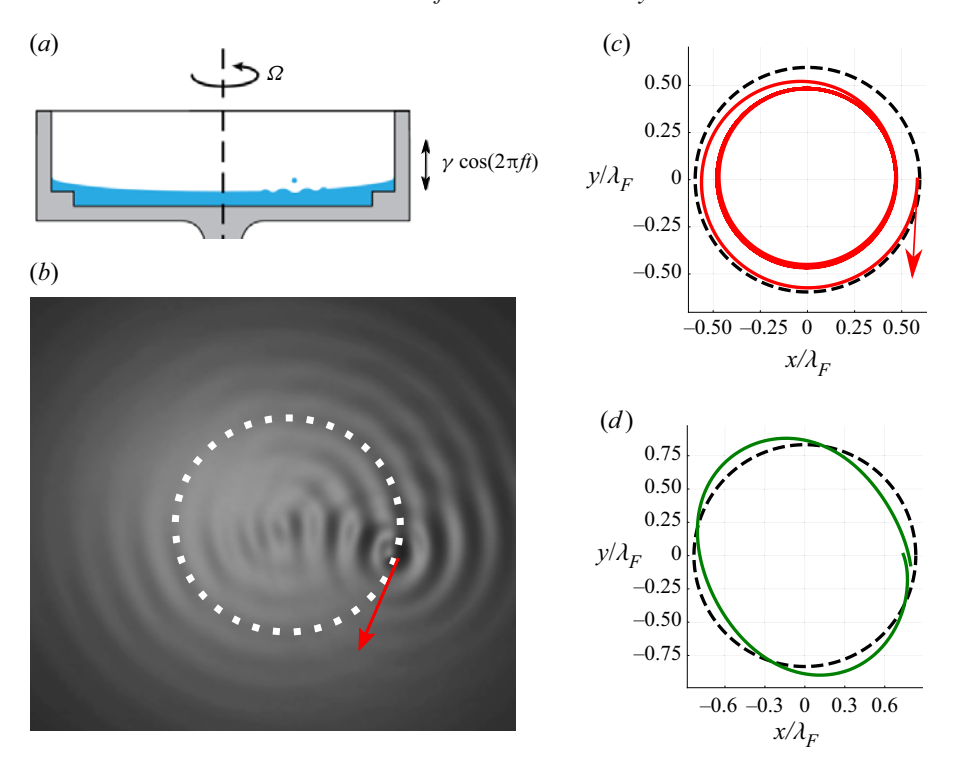


Figure 1. (a) A schematic illustration of the physical system of interest, millimetric droplets walking on the surface of a liquid bath vibrating vertically with acceleration $\gamma\cos(2\pi ft)$ and rotating about the vertical axis with angular frequency Ω . (b) In the rotating frame, the droplets may execute anticyclonic inertial circular orbits, in which the dominant force balance is between the outward inertial force and the inward Coriolis force. This force balance is augmented by the wave force, which at high memory may give rise to orbits that are quantised in radius (Fort et al. 2010; Harris & Bush 2014; Oza et al. 2014a). The wave field generated by the walking droplet has a characteristic wavelength corresponding to the Faraday wavelength λ_F . As the memory is increased progressively, these orbits may go unstable via one of two mechanisms. (c) A circular orbit (black dashed circle) of radius $r_0/\lambda_F = 0.60$ destabilises by a monotonic instability (red) characterised by initially exponential monotonic divergence from the circular path, the result being an orbit of smaller radius. (d) A circular orbit (black dashed circle) of radius $r_0/\lambda_F = 0.83$ destabilises into a wobbling orbit (green), characterised by a wobbling frequency of approximately twice the orbital frequency, known as a 2-wobble. In (c,d), the dimensionless vibration parameter $\Gamma = (\gamma - \gamma_W)/(\gamma_F - \gamma_W)$ takes values (c) $\Gamma = 0.7$ and (d) $\Gamma = 0.8$, where γ_W and γ_F are the walking and Faraday thresholds, respectively. Images (a,b) are adapted from Harris & Bush (2014).

Harris & Bush (2014) revisited droplets walking in a rotating frame experimentally, and focused on the destabilisation of the quantised orbits and the onset of chaos as the memory is increased progressively. They demonstrated the emergence of wobbling (see figure 1d), drifting, wobble-and-leap motions, and erratic trajectories at high path memory. In the long-path-memory limit, all circular orbits are unstable, and the droplet transitions intermittently between different quantised circular orbits; thus the histogram of the droplet's radius of curvature is multimodal, with peaks at the orbital radii of the quantised circular orbits. The emerging physical picture in this and other pilot-wave hydrodynamic systems is one of a droplet exciting then navigating its own potential (Bush & Oza 2020).

The theoretical modelling of the walking droplet system developed by Moláček & Bush (2013*a*,*b*) formed the basis of the stroboscopic model (Oza, Rosales & Bush 2013;

Oza *et al.* 2014*a*), in which the walking droplet is treated as a continuous source of monochromatic waves. The stroboscopic model has been successful in rationalising a number of features of the hydrodynamic pilot-wave system, including the destabilisation of a bouncing droplet into a walker, and the stability of various static and dynamic bound states (Bush & Oza 2020). Oza *et al.* (2014*a*) used the stroboscopic model to analyse droplets walking in a rotating frame, and rationalised the onset of orbital quantisation in terms of orbital instability at certain radii. Moreover, simulation of the stroboscopic model in a rotating frame revealed a variety of wobbling, drifting and quasi-periodic trajectories (Oza *et al.* 2014*b*) consistent with experimental observations reported by Harris & Bush (2014). Both experimental and theoretical studies report that at the onset of wobbling, the wobbling frequency is approximately twice the orbital frequency (Harris & Bush 2014; Oza *et al.* 2014*b*). We rationalise such resonant instabilities herein.

Several connections between stability and system energy have been proposed in the context of pilot-wave hydrodynamics. In particular, several investigations have suggested that the wave field energy is decreased at the onset of several instabilities, including the transition from bouncing to walking states (Durey & Milewski 2017), the transition from parallel walkers to promenading pairs (Borghesi *et al.* 2014; Durey & Milewski 2017), and the destabilisation of periodic orbits in a harmonic potential (Durey 2018; Durey, Milewski & Bush 2018). Moreover, the stability of droplet lattices appears to be related to the height of the local wave field averaged across all droplets in the lattice, a proxy for the mean droplet gravitational potential energy (Couchman & Bush 2020; Thomson, Durey & Rosales 2020). Finally, it has been suggested that the onset of orbital instability in a harmonic potential is controlled by the relative energy contribution of a small number of wave modes (Labousse *et al.* 2016a). Here, we assess the value of these energy-based arguments for predicting the instability of orbital walker motion on a rotating bath.

The mean wave field in pilot-wave hydrodynamics has proven to be a useful diagnostic for interpreting both the dynamical and statistical behaviour of walking droplets; moreover, it is of particular interest given its proposed relation to the quantum potential in Bohmian mechanics (Bush & Oza 2020). The influence of the mean pilot wave on the droplet dynamics has been explored in a number of settings, including the quantisation of circular and exotic orbits arising in a harmonic potential (Labousse 2014; Perrard *et al.* 2014*b*). The connection between the mean pilot wave and the emergent droplet statistics was first reported in an experimental study of walker motion in an elliptical corral (Sáenz *et al.* 2018), and a mathematical link between the two developed by Durey *et al.* (2018, 2020*a*). Here, we demonstrate the utility of the mean pilot-wave field as a diagnostic for orbital stability in a rotating frame.

We present herein a theoretical investigation of the orbital instability of a droplet walking in a rotating frame. We introduce the stroboscopic pilot-wave model in § 2, and determine an alternative formulation for the orbital stability problem in terms of various integrals that specify the influence of the system's path memory. In § 3, we deduce analytical expressions for the critical memory at the onset of orbital instability, and also rationalise the form of instability. For the case of wobbling instabilities, the associated wobbling frequency is deduced. In § 4, we compare the efficacy of various heuristic arguments for the onset of orbital instability and introduce a more insightful heuristic based on consideration of the mean wave field. Finally, in § 5, we discuss the implications of our findings for a broader class of orbital pilot-wave systems.

2. Pilot-wave hydrodynamics

We consider the motion of a millimetric drop of mass m self-propelling along the surface of a liquid bath vibrating vertically with frequency f and acceleration $\gamma \cos(2\pi ft)$ (see figure 1a). The system is subject to a vertical gravitational acceleration $-ge_z$ and rotates about a vertical axis with angular velocity $\Omega = \Omega e_z$, where e_z is the vertical unit vector. When the vibrational acceleration exceeds the Faraday threshold, $\gamma > \gamma_F$, the bath spontaneously destabilises to subharmonic Faraday waves with period $T_F = 2/f$ and wavelength $\lambda_F = 2\pi/k_F$ prescribed by the water-wave dispersion relation (Benjamin & Ursell 1954). The parameter regime of interest is $\gamma < \gamma_F$, where the fluid bath would remain quiescent in the absence of the droplet. For vibrational acceleration beneath the bouncing threshold, $\gamma < \gamma_B$, the droplet coalesces into the bath; however, for $\gamma > \gamma_B$, it bounces in place on the free surface. As γ is increased further, the drop achieves resonance with the bath, bouncing at the Faraday frequency. Beyond the walking threshold, $\gamma > \gamma_W$, this resonant bouncing state destabilises into a dynamic walking state, and the walking droplet generates a quasi-monochromatic wave field with the Faraday wavelength. The wave decay time T_M depends on the proximity to the Faraday threshold, specifically $T_M = T_d/(1 - \gamma/\gamma_F)$, where T_d is the viscous decay in the absence of vibrational forcing (Moláček & Bush 2013b). The memory parameter $M_e = T_M/T_F$ prescribes the number of prior impacts relevant to the dynamics. In the absence of system rotation, the droplet follows a rectilinear path at constant speed, u_0 . In the rotating frame, the droplet instead executes anticyclonic inertial orbits with radius r_0 and angular frequency ω .

A key notion in our study is that of orbital memory, M_e^O , the ratio of the memory time T_M to the orbital period $2\pi/\omega$, which prescribes the extent to which the orbiting drop interacts with its own wake (Oza et al. 2014a). When $M_e^O\gg 1$, the pilot wave decays over several orbital periods, the droplet interacts significantly with its own wake, and its trajectory is strongly influenced by its history. It is in the regime of intermediate orbital memory, $M_e^O\sim O(1)$, that orbital instability first arises, and so will be a focus of our study. When $M_e^O\ll 1$, the droplet is unperturbed by its wake, and instability emerges in the form of in-line speed oscillations that may arise for the rectilinear trajectory of a free walker (Bacot et al. 2019; Hubert et al. 2019; Durey, Turton & Bush 2020b).

We root our discussion in the parameter regime explored by Harris & Bush (2014), who used a fluid of density 949 kg m^{-3} , kinematic viscosity 20 cSt, surface tension 0.0206 N m^{-1} and depth 4 mm, with vibrational frequency f = 80 Hz, and a droplet of radius 0.4 mm whose free walking speed was approximately $u_0 = 11 \text{ mm s}^{-1}$.

2.1. Governing equations

To model the horizontal motion of the walker, we utilise the stroboscopic trajectory equation developed by Oza *et al.* (2013, 2014*a*), whereby the pilot-wave system is time-averaged over one bouncing period, $T_F = 2/f$ (Moláček & Bush 2013*b*). The droplet's horizontal position $x_p(t)$ thus evolves over time *t* according to (Oza *et al.* 2013, 2014*a*,*b*):

$$m\ddot{\mathbf{x}}_p + D\dot{\mathbf{x}}_p = -mg\,\nabla h(\mathbf{x}_p(t), t) - 2m\mathbf{\Omega} \times \dot{\mathbf{x}}_p. \tag{2.1a}$$

The drop is propelled by the wave force $-mg \nabla h(x_p(t), t)$, and also responds to the linear drag force $-D\dot{x}_p$ and the Coriolis force $-2m\Omega \times \dot{x}_p$. The accompanying pilot wave,

$$h(x,t) = \frac{A}{T_F} \int_{-\infty}^{t} J_0(k_F |x - x_p(s)|) e^{-(t-s)/T_M} ds,$$
 (2.1b)

Dimensionless parameters	Definition
$\kappa_0 = m/(DT_W)$	Inertia-to-drag ratio
$\hat{\Omega} = 2m\Omega/D$	Dimensionless rotation vector
$\mu = T_W/T_M$	Wave decay rate
$\Gamma = (\gamma - \gamma_W)/(\gamma_F - \gamma_W)$	Vibration parameter
r_0	Orbital radius, normalised by k_F^{-1}
ω	Orbital angular frequency
$\omega_{orb} = \omega/\mu$	Orbital memory parameter
$\omega_{orb} = \omega/\mu$ $\beta = \mu/\omega = \omega_{orb}^{-1}$	Inverse orbital memory parameter
$U = r_0 \omega$	Orbital speed
S	Asymptotic complex growth rate of perturbations
$S = \operatorname{Im}(s)$	Destabilisation frequency
$\xi = S/\omega$	Destabilisation frequency relative to orbital frequency

Table 1. The dimensionless parameters appearing in the pilot-wave system (2.2) and subsequent analysis.

is modelled as a continuous superposition of axisymmetric waves of amplitude A centred along the droplet's path, decaying exponentially in time over the memory time scale T_M . The quasi-monochromatic form of the pilot-wave field imposes a geometric constraint on the droplet's motion whose effects are most pronounced at high memory, where the Faraday waves are most persistent. The Faraday wavenumber, drag and wave amplitude parameters, respectively k_F , D and A, are defined in terms of physical quantities in Appendix A.

We project the pilot wave onto the droplet's path to yield an integro-differential trajectory equation for the droplet (Oza *et al.* 2013) that may be expressed in dimensionless variables as (Oza *et al.* 2014*a*; Oza, Rosales & Bush 2018)

$$\kappa_0 \ddot{\hat{\mathbf{x}}}_p + \dot{\hat{\mathbf{x}}}_p = 2 \int_{-\infty}^{\hat{t}} \frac{\mathbf{J}_1(|\hat{\mathbf{x}}_p(\hat{t}) - \hat{\mathbf{x}}_p(s)|)}{|\hat{\mathbf{x}}_p(\hat{t}) - \hat{\mathbf{x}}_p(s)|} (\hat{\mathbf{x}}_p(\hat{t}) - \hat{\mathbf{x}}_p(s)) e^{-\mu(\hat{t}-s)} ds - \hat{\mathbf{\Omega}} \times \dot{\hat{\mathbf{x}}}_p, \quad (2.2)$$

where $\hat{x}_p = k_F x_p$, $\hat{t} = t/T_W$, and $T_W = \sqrt{2DT_F/mgAk_F^2}$ is the memory time at the onset of walking, $\gamma = \gamma_W$ (Oza *et al.* 2013; Durey *et al.* 2020*b*). The dimensionless parameters $\mu = T_W/T_M > 0$ and $\kappa_0 = m/DT_W$ describe the wave decay rate and the relative importance of inertial and drag forces, respectively, and $\hat{\Omega} = 2m\Omega/D = \hat{\Omega}e_z$ is the dimensionless rotation vector (see table 1).

We characterise the pilot-wave dynamics in terms of the dimensionless vibration parameter $\Gamma = (\gamma - \gamma_W)/(\gamma_F - \gamma_W) = 1 - \mu$ (Bush 2015; Oza *et al.* 2018; Durey *et al.* 2020*b*), which increases with increasing path memory. We note that $\Gamma = 0$ corresponds to the walking threshold in the absence of a Coriolis force $(\gamma = \gamma_W)$, while $\Gamma = 1$ corresponds to the Faraday threshold $(\gamma = \gamma_F)$, and thus infinite path memory (Bush 2015). The experimental parameter regime of Harris & Bush (2014) corresponds to $\kappa_0 \approx 1.6$. We note that typically, κ_0 takes values in the range $0.8 \lesssim \kappa_0 \lesssim 1.6$ in the laboratory; likewise, the dimensionless rotation rate $\hat{\Omega}$ is restricted to the interval $0 \leq |\hat{\Omega}| \lesssim 1.3$ (Harris & Bush 2014; Oza *et al.* 2014*a*, 2018). Henceforth, we thus treat κ_0 and $\hat{\Omega}$ as O(1) quantities, whose influence on the pilot-wave dynamics we characterise through systematic asymptotic analysis.

2.2. Orbital dynamics

We characterise orbits in terms of their radius r_0 and angular frequency $\omega > 0$. By omitting hats and substituting $x_p(t) = r_0(\cos(\omega t), \sin(\omega t))$ into the trajectory equation (2.2), we express the radial and tangential force balances as (Oza *et al.* 2014*a*)

$$-\kappa_0 r_0 \omega^2 = 2 \int_0^\infty J_1\left(2r_0 \sin\left(\frac{\omega t}{2}\right)\right) \sin\left(\frac{\omega t}{2}\right) e^{-\mu t} dt + \Omega r_0 \omega, \tag{2.3a}$$

$$r_0\omega = 2\int_0^\infty J_1\left(2r_0\sin\left(\frac{\omega t}{2}\right)\right)\cos\left(\frac{\omega t}{2}\right)e^{-\mu t}dt,\tag{2.3b}$$

which may be solved for r_0 and ω given κ_0 , μ and Ω .

In our dimensionless notation, a suitable proxy for the orbital memory M_e^O is $\omega_{orb} = \omega/\mu$, which is the ratio of the wave decay time scale μ^{-1} to the orbital time scale $\omega^{-1} \sim r_0/u_0$, where u_0 is the steady walking speed in the absence of bath rotation (Oza *et al.* 2013; Durey *et al.* 2020*b*). The orbital speed $U = r_0\omega$ typically remains close to the free walking speed u_0 and satisfies $U < \sqrt{2}$ for all parameter values (see § 4.1). As U depends only weakly on the orbital radius at fixed memory, we note that $\omega_{orb} = U/(r_0\mu)$ decreases with increasing r_0 .

2.3. *Orbital stability*

In order to characterise the droplet's response to perturbations from a circular orbit, we apply linear stability analysis. Following the framework developed by Oza *et al.* (2014*a*), we linearise the trajectory equation (2.2) about the orbital solution expressed by (2.3). Specifically, we write

$$x_p(t) = r_p(t) \left(\cos \theta_p(t), \sin \theta_p(t) \right), \tag{2.4a}$$

where $r_p(t)$ and $\theta_p(t)$ are the time-varying radial and angular polar coordinates of the droplet's position, respectively. For a small perturbation from an orbital trajectory, we consider solutions of the form

$$r_p(t) = r_0 + \epsilon r_1(t)$$
 and $\theta_p(t) = \omega t + \epsilon \theta_1(t)$, (2.4b)

where r_0 and ω satisfy the orbital equations (2.3), and $\epsilon \ll 1$ is a small parameter. We substitute (2.4) into (2.2), retain terms to $O(\epsilon)$, and then take the Laplace transform of the resultant linear equations. It follows that the perturbed trajectory's asymptotic complex growth rates s satisfy F(s) = 0, where

$$F(s) = \mathcal{A}(s)\,\mathcal{D}(s) + \mathcal{B}(s)\,\mathcal{C}(s),\tag{2.5}$$

and the stability coefficients are defined (in a form equivalent to Oza et al. 2014a, 2018) as

$$\mathcal{A}(s) = \kappa_0(s^2 - 2\omega^2) + \mu + s - 2\Omega\omega + C_0(s) + \mathcal{I}_1(s) - 2\mathcal{I}_0(0), \tag{2.6a}$$

$$\mathscr{B}(s) = 2\kappa_0 \omega s + \Omega s - \mu(\kappa_0 \omega + \Omega) - \mathcal{S}_0(s), \tag{2.6b}$$

$$\mathscr{C}(s) = 2\kappa_0 \omega s + 2\omega + \Omega s + \mu(\kappa_0 \omega + \Omega) - S_0(s), \tag{2.6c}$$

$$\mathscr{D}(s) = \kappa_0 s^2 + s - \mu + \mathcal{C}_0(s) - \mathcal{I}_1(s). \tag{2.6d}$$

Of particular interest in our investigation are the integrals (defined for $Re(s) > -\mu$ and any integer $m \ge 0$)

$$\mathcal{I}_m(s) = \int_0^\infty J_{2m} \left(2r_0 \sin\left(\frac{\omega t}{2}\right) \right) e^{-(\mu + s)t} dt, \qquad (2.7a)$$

$$C_m(s) = \int_0^\infty J_{2m} \left(2r_0 \sin\left(\frac{\omega t}{2}\right) \right) \cos(\omega t) e^{-(\mu + s)t} dt, \qquad (2.7b)$$

$$S_m(s) = \int_0^\infty J_{2m} \left(2r_0 \sin\left(\frac{\omega t}{2}\right) \right) \sin(\omega t) e^{-(\mu + s)t} dt, \qquad (2.7c)$$

which encode the effects of memory on the stability problem, and present most of the difficulty in solving the stability problem analytically. One important contribution of our study is the exact analytical evaluation of the stability integrals (2.7) in terms of Bessel functions of complex order. Specifically, we derive in Appendix B the closed-form expression

$$\mathcal{I}_{m}(s) = -\frac{\pi}{\omega} J_{m+i\eta}(r_0) J_{m-i\eta}(r_0) \operatorname{csch}(\pi \eta), \qquad (2.8)$$

where $\eta = (\mu + s)/\omega$. Moreover, by representing $\cos(\omega t)$ and $\sin(\omega t)$ in terms of complex exponential functions, we deduce that

$$C_m(s) = \frac{1}{2} \left(\mathcal{I}_m(s + i\omega) + \mathcal{I}_m(s - i\omega) \right) \quad \text{and} \quad S_m(s) = \frac{1}{2i} \left(\mathcal{I}_m(s - i\omega) - \mathcal{I}_m(s + i\omega) \right),$$
(2.9a,b)

which we use to derive similar closed form formulae for C_m and S_m . Using (2.8)–(2.9a,b), we derive in Appendix B simplified expressions for each of the stability integrals appearing in (2.6) in terms of products of Bessel functions of the first kind, $J_{\nu}(r_0)$, and their derivatives $J'_{\nu}(r_0)$, where the complex order ν takes values $\nu \in \{\pm i(\mu + s)/\omega\}$. We then utilise asymptotic expansions of each integral evaluation to characterise orbital instability (§ 3).

Motivated by our exact analytical evaluation of the stability integrals, we seek to recast the force balance equations (2.3) in a similar manner. To simplify our investigation, we parametrise the orbital dynamics entirely in terms of the radius r_0 (Oza 2014), thereby effectively eliminating Ω from the stability problem. This elimination process is achieved by first recasting the radial force balance (2.3a) as

$$\Omega = -\kappa_0 \omega - \frac{2}{r_0 \omega} \int_0^\infty J_1\left(2r_0 \sin\left(\frac{\omega t}{2}\right)\right) \sin\left(\frac{\omega t}{2}\right) e^{-\mu t} dt, \qquad (2.10)$$

where we observe that the integral in (2.10) may be expressed as

$$\int_0^\infty J_1\left(2r_0\sin\left(\frac{\omega t}{2}\right)\right)\sin\left(\frac{\omega t}{2}\right)e^{-\mu t}dt = -\frac{1}{2}\frac{\partial \mathcal{I}_0(0)}{\partial r_0}.$$
 (2.11)

By combining (2.10) and (2.11), we eliminate Ω in the stability coefficients (2.6), yielding

$$\mathscr{A}(s) = \kappa_0 s^2 - \frac{2}{r_0} \frac{\partial \mathcal{I}_0(0)}{\partial r_0} - 2I_0(0) + \mu + s + \mathcal{C}_0(s) + \mathcal{I}_1(s), \tag{2.12a}$$

$$\mathscr{B}(s) = \kappa_0 \omega s - \frac{\mu - s}{r_0 \omega} \frac{\partial \mathcal{I}_0(0)}{\partial r_0} - \mathcal{S}_0(s), \tag{2.12b}$$

$$\mathscr{C}(s) = \kappa_0 \omega s + 2\omega + \frac{\mu + s}{r_0 \omega} \frac{\partial \mathcal{I}_0(0)}{\partial r_0} - \mathcal{S}_0(s), \tag{2.12c}$$

$$\mathscr{D}(s) = \kappa_0 s^2 + s - \mu + \mathcal{C}_0(s) - \mathcal{I}_1(s). \tag{2.12d}$$

Finally, we reduce the tangential force balance by integrating (2.3b) by parts, from which it follows that the orbital speed $U = r_0 \omega$ satisfies (Oza et al. 2014a)

$$\mathcal{I}_0(0) = \frac{1}{\mu} \left(1 - \frac{r_0^2 \omega^2}{2} \right). \tag{2.13}$$

For any given $r_0 > 0$, the orbital stability problem may be expressed solely in terms of the reduced tangential force balance (2.13) and the stability condition F(s) = 0, both of which are defined in terms of the stability integrals (2.7).

The orbital solution is unstable if there are any roots s of F satisfying Re(s) > 0. By denoting s_* as the unstable root with largest real part, the instability is monotonic if $Im(s_*) = 0$, and oscillatory otherwise. The stability function F has trivial eigenvalues at 0 and $\pm i\omega$, corresponding to rotational and translational invariance of the orbital motion, respectively (Oza *et al.* 2014a). It follows, therefore, that the non-trivial roots of the stability problem satisfy G(s) = 0, where

$$G(s) = \frac{\mathscr{A}(s)\,\mathscr{D}(s) + \mathscr{B}(s)\,\mathscr{C}(s)}{s(s^2 + \omega^2)}.$$
(2.14)

We apply the method of Delves & Lyness (1967) to find the roots of G in the domain over which G is analytic, i.e. $Re(s) > -\mu$. To ascertain whether a particular orbital state is stable or unstable, typically we utilise a rectangular integration contour spanning the domain $Re(s) \in [0, 20]$ and $Im(s) \in [0, 5]$, which we find to be sufficient for identifying all roots with a positive real part across the experimentally based parameter regime considered in this study $(0 \le \Gamma \le 0.99)$. This approach differs from that of Oza *et al.* (2018), who instead applied the methodology of Delves & Lyness (1967) to F, integrating F'/F over a deformed contour specifically chosen to avoid the trivial zeros at s = 0 and $s = \pm i\omega$. The method presented here instead removes the singularities analytically, thereby avoiding contour deformations near the trivial zeros of F; however, local Taylor series approximations are necessary to avoid numerical difficulties arising sufficiently close to the removable singularities of G.

In figure 2(a), we follow Oza *et al.* (2014*a*, 2018) in presenting the dependence of the orbital radius on the bath rotation rate for $\Gamma = 0.8$. In figure 2(b), we summarise the stability behaviour for all Γ . As path memory is increased progressively, stable circular orbits (blue) destabilise via either a monotonic (red, see figure 1c) or oscillatory (green, see figure 1d) instability mechanism. Associated monotonic (red) and oscillatory (green) instability 'tongues' emerge in the stability diagram, with the tip of each tongue corresponding to the onset of a new instability. The blue regions between the instability tongues correspond to regions of orbital quantisation. Notably, as memory is increased beyond the tip of an oscillatory instability tongue, the orbital instability typically manifests

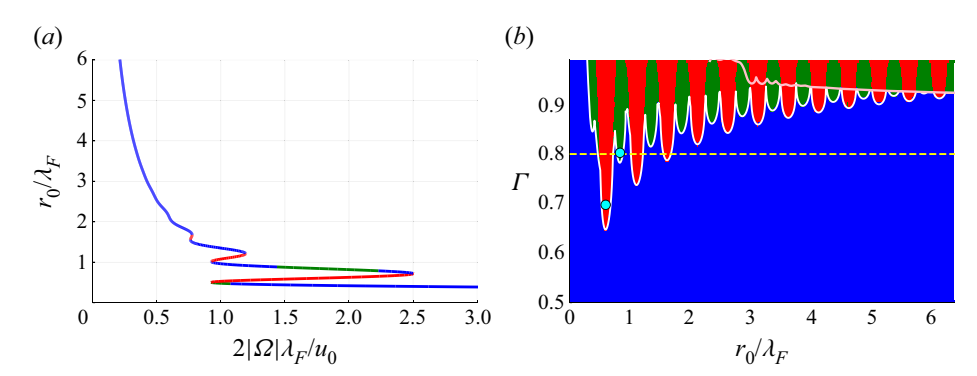


Figure 2. Orbital stability and the onset of quantisation for $\kappa_0=1.6$, where $\kappa_0=m/(DT_W)$ is the inertial coefficient appearing in (2.2). (a) The dependence of orbital radius on bath rotation rate for $\Gamma=0.8$, where $\Gamma=(\gamma-\gamma_W)/(\gamma_F-\gamma_W)$ is the dimensionless vibration parameter. (b) The delineation of orbital stability for any given radius and memory. The stability boundary is highlighted in white, and the yellow line at $\Gamma=0.8$ corresponds to the curve in (a). In both plots, stable orbital states are indicated in blue, while oscillatory and monotonic instabilities are highlighted in green and red, respectively. We note that in (b), the instability tongues alternate between monotonic and wobbling as the orbital radius is increased progressively. The cyan dots in the red and green regions denote the parameters corresponding to the monotonic and wobbling trajectories presented in figures 1(c,d). The pink curve denotes an instability related to in-line speed oscillations of the order of the Faraday wavelength (Durey *et al.* 2020*b*), which is subdominant for $r_0/\lambda_F \lesssim 4$, and truncates the instability tongues for $r_0/\lambda_F \gtrsim 4$.

as a wobbling orbit, in which the orbital centre remains approximately constant, but the radius of curvature exhibits small-amplitude oscillations with a frequency approximately twice that of the orbital frequency, as reported in the experiments of Harris & Bush (2014) and the numerical simulations of Oza *et al.* (2014b) (see figure 1d). Furthermore, the instability tongues appear to have a periodic structure, with the critical memory increasing with increasing orbital radius. We observe that the monotonic and wobbling instability tongues are nested, with monotonic instability tongues forming at lower memory than the neighbouring wobbling instability tongues.

2.4. The onset of instability: asymptotic scaling relationships

Although the stability integrals (2.7) may be evaluated analytically (see (2.8)–(2.9a,b)), the purpose of this subsection is to motivate the asymptotic scaling relationships arising near the tip of each instability tongue. In particular, we determine the main contributions to each stability integral arising along a stability boundary (s = iS with S real) for large orbital radius ($r_0 \gg 1$), for which each integrand is highly oscillatory. Using (2.9a,b) to express C_m and S_m in terms of I_m , we henceforth focus our attention on the study of I_m . Furthermore, by recognising that I_m is a Laplace transform of a periodic function, we reduce the integral (2.7a) to

$$\mathcal{I}_{m}(iS) = \frac{\mathcal{L}_{m}(\xi)}{\omega \left(1 - e^{-2\pi(\beta + i\xi)}\right)}, \quad \text{where } \mathcal{L}_{m}(\xi) = \int_{0}^{2\pi} J_{2m} \left(2r_{0} \sin\left(\frac{\theta}{2}\right)\right) e^{-(\beta + i\xi)\theta} d\theta.$$
(2.15)

Here, $\beta = \mu/\omega$ is the inverse orbital memory, and $\xi = S/\omega$ is the scaled destabilisation frequency (see table 1). Based on experimental and numerical observations of monotonic and wobbling instabilities (Harris & Bush 2014; Oza *et al.* 2014*b*), we assume henceforth that the destabilisation frequency is comparable to the orbital frequency (i.e. $\xi = O(1)$). Notably, our analysis does not account for the instability associated with in-line speed

oscillations arising at larger orbital radii (denoted by the pink curve in figure 2b), for which $S \sim U$, or $\xi \sim r_0$ (Durey *et al.* 2020*b*). Finally, by writing $\beta = \mu r_0/U$ and noting that μ at the tip of successive wobbling (or successive monotonic) instability tongues decreases with increasing orbital radius (see figure 2b), we deduce that the magnitude of β is at most of $O(r_0)$ when the orbital radius is large (since U = O(1) for all orbital radii). Our analysis in this subsection determines the precise scaling relationship between β and r_0 , namely $\beta = O(\ln r_0)$, where \ln denotes the natural logarithm.

Before proceeding with the asymptotic expansions, we provide a physical interpretation for the integral $\mathcal{L}_m(\xi)$. The argument $2r_0\sin(\theta/2) \geq 0$ is the length of the chord spanning two points lying an angle θ apart on a circle of radius r_0 . This distance reflects the influence of the droplet's path memory on the evolution of the perturbed trajectory, where the extent of the path memory is controlled by the damping rate $\beta > 0$. Notably, $e^{-\pi\beta}$ is the wave damping factor over half an orbital period, which accounts for the contribution of waves generated when the droplet was last diametrically opposite its current position; likewise, $e^{-2\pi\beta}$ determines the wave damping factor over a complete orbital period. Finally, the factor $e^{-i\xi\theta}$ accounts for oscillations in the perturbed droplet trajectory. For large r_0 , the integrand of $\mathcal{L}_m(\xi)$ is generally highly oscillatory, with dominant contributions arising over non-oscillatory intervals centred about critical points; these critical points are either internal points of stationary phase, or boundary points arising when the argument of J_{2m} vanishes, i.e. at $\theta = 0$ and $\theta = 2\pi$ (Bleistein & Handelsman 1975). The internal points of stationary phase arise when the argument of the Bessel function is stationary, i.e. at $\theta = \pi$. We now proceed to determine the magnitude of the contribution made by each critical point.

We first examine the contributions to \mathcal{L}_m arising about $\theta=0$ and $\theta=2\pi$, which we denote by $\mathcal{L}_{m,0}$ and $\mathcal{L}_{m,2\pi}$, respectively. We derive in Appendix C the leading-order contribution $\mathcal{L}_{m,0}=O(r_0^{-1})$, which is valid when $\xi=O(1)$ and β is of maximum size $O(r_0)$; both of these conditions are met near the tip of each instability tongue. Using the structure of the integrand of $\mathcal{L}_m(\xi)$, we determine similarly that the leading-order contribution about $\theta=2\pi$ satisfies $\mathcal{L}_{m,2\pi}(\xi)=\mathrm{e}^{-2\pi(\beta+\mathrm{i}\xi)}\mathcal{L}_{m,0}(\xi)$; thus the relative size of $\mathcal{L}_{m,0}(\xi)$ and $\mathcal{L}_{m,2\pi}(\xi)$ is controlled by the orbital damping factor $\mathrm{e}^{-2\pi\beta}$. Finally, we use the method of stationary phase (see Appendix C) to determine that the interior point contribution to \mathcal{L}_m at π has magnitude

$$\mathcal{L}_{m,\pi} = O\left(\frac{\mathrm{e}^{-\pi\beta}}{r_0}\right). \tag{2.16}$$

The relative weight of the integral contributions about $\theta=0$, π and 2π seemingly decreases consecutively by a factor $e^{-\pi\beta}$. However, the contribution about $\theta=\pi$ becomes significant when $e^{\pi\beta}$ scales algebraically with r_0 , corresponding to a strong influence of the waves generated diametrically opposite the droplet's current position, as is characteristic of high orbital memory (Fort *et al.* 2010). Indeed, as is evident in figure 3, the tips of each instability tongue, both monotonic (red line) and oscillatory (green line), satisfy the asymptotic scaling relationship $e^{\pi\beta} = O(r_0^2)$, which motivates the asymptotic scaling relationships utilised in the forthcoming analysis (§ 3). In fact, we observe that each instability tongue is bounded above in memory by either the oscillatory instability threshold satisfying $e^{\pi\beta} = O(r_0)$ (gold dashed line), or the in-line speed oscillation instability threshold (purple dashed line) arising for free walkers (Bacot *et al.* 2019; Hubert *et al.* 2019; Durey *et al.* 2020*b*). Detailing the latter instability (denoted by the pink curve in figure 2*b*), which manifests as in-line speed oscillations along the circular orbit with

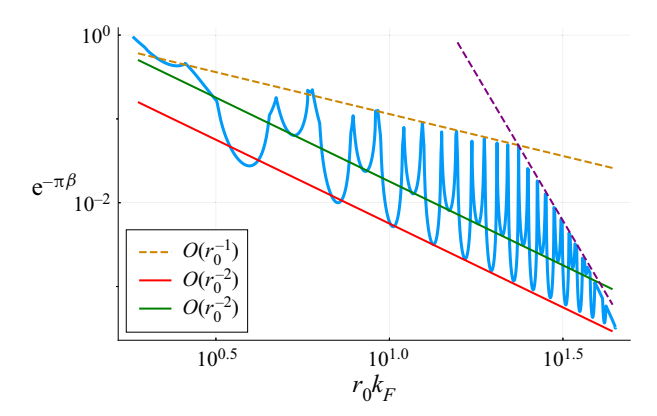


Figure 3. Envelopes of the stability boundary, the scalings of which are deduced from our stationary phase analysis (see § 2.4). The blue curve corresponds to the white stability boundary in figure 2(b). The green and red lines correspond to the wobbling and monotonic instability envelopes. The gold and purple dashed lines denote the upper bounds on the existence of stable circular orbits, corresponding to the transition from wobbling to monotonic instabilities, and the onset of in-line speed oscillations (pink curve in figure 2b), respectively. The half-orbit wave damping factor $e^{-\pi\beta}$ scales as $(r_0k_F)^{-2}$ for the green and red lines, and as $(r_0k_F)^{-1}$ for the gold line.

amplitudes of the order of the Faraday wavelength, and arises for orbits so large as to be inaccessible within the laboratory, will be the subject of a future investigation.

3. The onset of instability

In figure 4, we compare the scaled destabilisation frequency $\xi = S/\omega$, computed along the stability boundary for the first wobbling instability tongue (see figure 2b), to that of nonlinear wobbling states arising just beyond the instability threshold (see figure 1d), as reported in the experimental study of Harris & Bush (2014) and the numerical simulations of Oza et al. (2014b). The nonlinear wobbling frequency remains close to that predicted by the linear stability analysis, with the two coinciding in the small-wobbling-amplitude limit. Furthermore, both frequencies remain close to twice the orbital frequency, which serves to further motivate our analysis of resonant wobbling instabilities. We proceed to elucidate these observations by means of systematic asymptotic analysis performed along the stability boundary. Our analysis will also rationalise the quasi-periodicity and envelopes of the instability tongues, and the influence of the inertial coefficient κ_0 on orbital stability.

We characterise the onset and form of each instability tongue using asymptotic analysis valid when $r_0 \gg 1$. For wobbling instabilities, the destabilisation frequency S is comparable to the orbital frequency ω ; thus we assume that the dimensionless wobbling frequency is $\xi = S/\omega = O(1)$. Moreover, the dimensionless orbital speed $U = r_0\omega$ typically remains close to the free walking speed $u_0 = O(1)$ (Durey *et al.* 2020*b*). We thus replace ω with U/r_0 in the stability equations (2.12) and tangential force balance (2.13), and henceforth assume U = O(1). The dependence of the orbital memory ω_{orb} on the orbital radius is more subtle. As motivated in § 2.4 and evidenced in figure 3, the tip of each instability tongue is characterised by the scaling relationship $e^{\pi\beta} = O(r_0^2)$ (where $\beta = \omega_{orb}^{-1}$), which represents the key dominant balance underpinning our asymptotic analysis. Notably, this dominant balance implies that the orbital memory

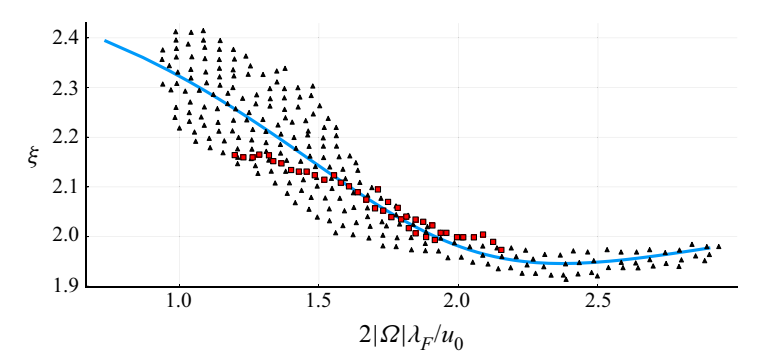


Figure 4. The dependence of the ratio of the wobbling frequency to the orbital frequency ξ on the bath rotation rate Ω , just beyond the onset of instability for the first wobbling tongue in figure 2(*b*). Data indicating the wobbling frequencies are reported in the experimental study of Harris & Bush (2014, figure 7*b*) (red squares, 0.961 $\leq \gamma/\gamma_F \leq$ 0.978) and the numerical simulations of Oza *et al.* (2014*b*, figures 2*c*,*d*) (black triangles, 0.952 $\leq \gamma/\gamma_F \leq$ 0.967), corresponding to $\kappa_0 = 1.6$, where $\kappa_0 = m/DT_W$. The blue curve indicates our prediction for the wobbling frequency along the stability boundary (white curve in figure 2*b*), corresponding to the small-wobbling-amplitude limit.

generally decreases with increasing orbital radius, such that $\omega_{orb} \sim (\ln(r_0))^{-1}$ when $r_0 \gg 1$.

3.1. Asymptotic expansion

We proceed by using the asymptotic expansions of the integrals in (2.12) to identify the imaginary roots of the stability function G defined in (2.14) when $r_0 \gg 1$. Specifically, we seek the roots that minimise the critical memory of instability, which arise along the stability boundary in figure 2(b). We utilise asymptotic expansions for the closed-form expressions of the stability integrals (see Appendix B), which involve Bessel functions $J_{\nu}(r_0)$ of the first kind with complex order ν , and their derivatives with respect to argument $J'_{\nu}(r_0)$ (see (B7)). As the complex order takes values $\nu \in \{\pm i\beta, \pm i(\beta \pm i\xi)\}$ along the stability boundary, where $\beta = O(\ln(r_0))$ and $\xi = O(1)$ for $r_0 \gg 1$, the argument of each Bessel function is asymptotically large relative to its order. We may thus expand each of the stability coefficients in (2.12) when $r_0 \gg 1$, utilising the dominant balance $e^{\pi\beta} = O(r_0^2)$, with details presented in Appendix D. Likewise, we use the large-argument expansions of the Bessel functions, valid when $\beta = O(\ln(r_0)) \ll \sqrt{r_0}$, to deduce that

$$U^{2} = 2\left(1 - \frac{\beta}{r_{0}}\right) + O\left(\frac{1}{r_{0}^{3}}\right),\tag{3.1}$$

which will be utilised throughout the following analysis.

As our aim is to identify the imaginary roots of the equation G(s) = 0, we proceed by substituting the asymptotic approximations expressed in (D2) into (2.14). Moreover, we determine the orbital speed U, scaled destabilisation frequency ξ , and inverse orbital memory β , by means of an asymptotic expansion in terms of the small parameter r_0^{-1} , namely

$$U = U_0 + \frac{U_1}{r_0} + O\left(\frac{1}{r_0^2}\right), \quad \xi = \xi_0 + \frac{\xi_1}{r_0} + O\left(\frac{1}{r_0^2}\right), \quad \beta = \beta_0 + \frac{\beta_1}{r_0} + O\left(\frac{1}{r_0^2}\right). \tag{3.2a-c}$$

In § 3.2, we present the solution to the leading-order problem, for which we demonstrate systematically that $\xi = 2 + O(r_0^{-2})$ at the tip of each wobbling instability tongue, corresponding to a wobbling instability with wobbling angular frequency 2ω , the so-called 2-wobble (Harris & Bush 2014; Oza *et al.* 2014*b*; see figure 2) and find the critical memory for wobbling and monotonic instabilities. To determine how the scaled destabilisation frequency varies away from the tip of each wobbling instability tongue, we extend the asymptotic procedure to incorporate higher-order corrections in § 3.3.

3.2. Leading-order solution

We proceed to determine the leading-order solution, corresponding to the values of U_0 , ξ_0 and β_0 . By using the asymptotic relationship $\mathcal{D} = i\xi \mathcal{C} + O(r_0^{-3})$ deduced in (D2), we find that the stability condition (2.14) satisfies

$$\frac{\mathscr{C}(\mathrm{i}\xi\mathscr{A} + \mathscr{B})}{\mathrm{i}\xi(\xi^2 - 1)} = O\left(\frac{1}{r_0^4}\right),\tag{3.3}$$

whereupon substituting the leading-order expressions for \mathcal{A} , \mathcal{B} , U, ξ and β from (D2) and (3.2a-c) results in

$$\frac{\mathscr{C}}{U_0} \left[\frac{2\sin(2r_0)}{\xi_0^2 - 1} \left(\operatorname{csch}(\pi(\beta_0 + i\xi_0)) + \operatorname{csch}(\pi\beta_0) \right) + \frac{\kappa_0 U_0^3 + 1}{r_0^2} \right] = O\left(\frac{1}{r_0^3}\right). \tag{3.4}$$

As $\mathscr{C} = 2U_0/r_0 + O(r_0^{-2})$ is non-zero to leading order (see (D2)), the leading-order solution to (3.4) may be found by setting the term in square brackets equal to zero. Furthermore, the imaginary part of (3.4) can be satisfied only when the destabilisation frequency ξ_0 is an integer, whose possible values will be the focus of the remainder of this subsection. We proceed to eliminate possible integer values for ξ_0 by looking for the solutions to the stability problem that occur at the highest possible value of β_0 , as these solutions correspond to the instabilities arising at lowest memory for a given orbital radius. Our analysis will show that only two solutions are possible: (i) $\xi_0 = 0$, corresponding to a monotonic instability; and (ii) $\xi_0 = 2$, corresponding to a 2ω instability.

To explore the possibility of ξ_0 being odd, we first consider the limit $\xi_0 \to 1$ in (3.4). By applying L'Hôpital's rule, we find that the leading-order stability condition reduces to

$$1 + \kappa_0 U_0^3 + i\pi r_0^2 \sin(2r_0) \coth(\pi \beta_0) \operatorname{csch}(\pi \beta_0) = 0.$$
 (3.5)

As the real parts cannot be balanced (since $U_0 > 0$), there are no solutions to this equation. Similarly, if ξ_0 were odd and not equal to 1, the leading-order stability condition (3.4) would become

$$1 + \kappa_0 U_0^3 = 0, (3.6)$$

which is also impossible to satisfy. We thus conclude that ξ_0 cannot be odd, meaning that the destabilisation frequency must be an even multiple of the orbital frequency.

To explore the possible even values of ξ_0 , we denote $\xi_0 = 2n$ (where n is an integer) and use the approximation $\sinh(x) \approx \cosh(x) \approx \frac{1}{2} e^x$ for $x \gg 1$; as such, the leading-order stability condition (3.4) reduces to

$$e^{\pi\beta_0} = \frac{8r_0^2 \sin(2r_0)}{(1 - 4n^2)(1 + \kappa_0 U_0^3)}.$$
(3.7)

To be consistent with the assumed scaling of $e^{\pi\beta_0} = O(r_0^2)$, we require $\sin(2r_0) = O(1)$. As $\sin(2r_0)$ can be either positive or negative, the lowest memory (or largest β_0) condition

requires maximising the magnitude of the right-hand side of (3.7). In the case n = 0, we have a monotonic instability: by noting that $U_0 = \sqrt{2}$ from (3.1) and (3.2*a*–*c*), we thus arrive at the monotonic stability boundary

$$\mu_{mon} = \frac{\sqrt{2}}{\pi r_0} \ln \left(\frac{8r_0^2 \sin(2r_0)}{1 + 2\sqrt{2}\kappa_0} \right),\tag{3.8}$$

which is valid when $\sin(2r_0) > 0$ and $\sin(2r_0) = O(1)$. For the case $n \neq 0$, we observe that $1 - 4n^2 < 0$; we thus deduce the requirement $\sin(2r_0) < 0$. The magnitude of the right-hand side of (3.7) is then minimised at n = 1, which corresponds to $\xi = 2$, or $s = 2i\omega$. We have thus demonstrated that the destabilisation frequency along wobbling stability boundaries is approximately twice the orbital angular frequency. By substituting n = 1 into (3.7) and rearranging, we deduce that the corresponding critical wave decay rate for a wobbling instability is

$$\mu_{wob} = \frac{\sqrt{2}}{\pi r_0} \ln \left(-\frac{8r_0^2 \sin(2r_0)}{3(1 + 2\sqrt{2}\kappa_0)} \right),\tag{3.9}$$

which is valid when $\sin(2r_0) < 0$ and $\sin(2r_0) = O(1)$.

The asymptotic expressions (3.8)–(3.9) for the instability memory give rise to alternation between wobbling $(\sin(2r_0) < 0)$ and monotonic $(\sin(2r_0) > 0)$ instabilities with increasing orbital radius. In addition, μ_{mon} and μ_{wob} are maximised (corresponding to the tip of each instability tongue) when, to leading order for large orbital radius, $\sin(2r_0) = 1$ and $\sin(2r_0) = -1$, respectively. These extrema thus determine the wobbling and monotonic envelopes

$$\mu_{wob}^{env} = \frac{\sqrt{2}}{\pi r_0} \ln \left(\frac{8r_0^2}{3(2\sqrt{2}\kappa_0 + 1)} \right) \quad \text{and} \quad \mu_{mon}^{env} = \frac{\sqrt{2}}{\pi r_0} \ln \left(\frac{8r_0^2}{2\sqrt{2}\kappa_0 + 1} \right), \quad (3.10a,b)$$

which are represented in figure 5(a) by the green and red dashed curves, respectively. Notably, increasing κ_0 increases the critical memory of wobbling and monotonic instabilities. Furthermore, since $\mu_{mon}^{env} - \mu_{wob}^{env} = \sqrt{2} \ln(3)/(\pi r_0) > 0$, we conclude that the envelope of the monotonic instabilities arises at a lower memory than that of wobbling instabilities, as evident from the red and green lines in figure 3.

3.3. First-order wobbling and monotonic solutions

The leading-order analysis presented in § 3.2 determined approximations for the wobbling frequency and the critical memory at onset of instability, from which we deduced the most unstable orbital radii. However, the leading-order analysis did not provide insight into the behaviour of the instability frequency along each wobbling tongue, specifically the extent to which wobbling instabilities are approximated by a 2-wobble. So as to investigate this behaviour and so determine U_1 , ξ_1 and β_1 , we proceed to solve the tangential force balance and the stability problem in (3.1) and (3.3) to next order by using the expansions in (3.2a–c). The expanded tangential force balance (D2) shows that $U_1 = -\beta_0/U_0$. By substituting into the stability condition i $\xi \mathcal{A} + \mathcal{B} = 0$, using (D2) and (3.2a–c), retaining next-order terms and solving for the real and imaginary parts, we deduce that wobbling

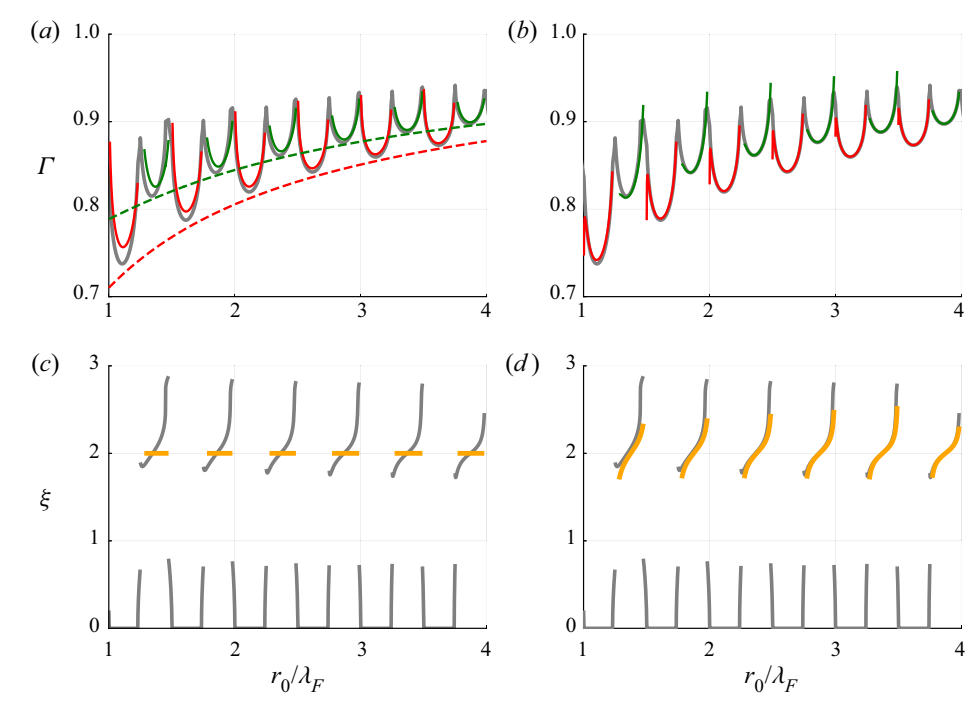


Figure 5. Comparison of the numerical solution and asymptotic approximations to the wobbling and monotonic stability boundaries. (a,b) The critical dimensionless vibration parameter at onset, $\Gamma = (\gamma - \gamma_W)/(\gamma_F - \gamma_W)$, and (c,d) the instability frequency relative to the orbital frequency, $\xi = S/\omega$, for $\kappa_0 = 1.6$. We compare the numerical solution (grey) with (a,c) the leading-order ((3.8)-(3.9)) and (b,d) the first-order ((3.10a,b)-(3.12)) asymptotic results. (a,b) The critical memory compared to the asymptotic wobbling (green) and monotonic (red) instability boundaries. In (a), the leading-order envelopes (3.10a,b) are denoted by dashed curves. (c,d) The critical wobbling frequency and its asymptotic counterpart (orange). All the asymptotic results presented in (a-d) are valid when $\sin(2k_Fr_0) = O(1)$, k_Fr_0 is large, and $\xi = 0$ (monotonic instabilities) or $\xi \approx 2$ (2-wobbles). Discontinuities in the grey curves (c,d) reflect transitions between monotonic $(\xi = 0)$ and wobbling $(\xi \approx 2)$ instabilities.

instabilities ($\xi_0 \neq 0$) have the first-order correction

$$\xi_1 = -\frac{4\beta_0}{\pi} \cot(2r_0) \quad \text{and} \quad \beta_1 = \frac{3\sqrt{2}\kappa_0\beta_0}{\pi(2\sqrt{2}\kappa_0 + 1)} + \left(\frac{64\beta_0 + 27\pi}{12\pi^2} - \frac{\beta_0^2}{\pi}\right) \cot(2r_0). \tag{3.11a,b}$$

Similarly, for the monotonic instability ($\xi_0 = 0$), one may deduce that $\xi_1 = 0$ and

$$\beta_1 = \frac{3\sqrt{2}\kappa_0\beta_0}{\pi(2\sqrt{2}\kappa_0 + 1)} + \left(\frac{2\pi\beta_0 + 1}{4\pi} - \frac{\beta_0^2}{\pi}\right)\cot(2r_0). \tag{3.12}$$

We recall that the asymptotic solution is valid when $\sin(2r_0) = O(1)$. Notably, ξ_1 vanishes for wobbling instabilities when $\cos(2r_0) = 0$, corresponding to $s = i\omega(2 + O(r_0^{-2}))$ at the most unstable orbital radii (see § 3.2). Wobbling instabilities are thus driven by a resonance between the destabilisation frequency and the orbital frequency, with a larger critical memory necessary to destabilise orbits whose instability frequency deviates from twice the orbital frequency.

3.4. Comparison to the numerical instability tongues

To buttress our asymptotic developments, we compare the numerically deduced instability tongues to our asymptotic formulae in figure 5, with leading-order results presented in figures 5(a,c) and first-order corrections in figures 5(b,d). Notably, our asymptotic results are valid when $r_0 \gg 1$, $\sin(2r_0) = O(1)$ and either $\xi = 0$ (corresponding to monotonic instabilities) or $\xi \approx 2$ (corresponding to wobbling instabilities). Despite these restrictions, the leading-order memory captures the main features of the stability tongues, and the asymptotic instability frequency closely matches the numerical behaviour for $\xi = 0$ or $\xi \approx 2$. The success of our asymptotic results even for orbits of moderate radius is rooted in the choice of expansion parameter, namely $k_F r_0$ in dimensional variables, which is assumed to be large. We note that all orbits presented in figure 5 satisfy $k_F r_0 \geq 2\pi$ (or $r_0/\lambda_F \geq 1$), which is evidently sufficiently large for our asymptotic results to yield reasonable agreement. Finally, we note that a similarly favourable agreement between our asymptotic and numerical results was obtained across a wide range of κ_0 values, including for those inaccessible in the laboratory (see § 4.1).

In summary, our asymptotic results explain the preponderance of 2-wobbles, with an exact resonance arising at the most unstable radius of each wobbling instability tongue. Moreover, we quantify the detuning from an exact resonance and the corresponding increase in the critical memory for nearby orbital radii. Finally, our asymptotic results demonstrate that the instability tongues alternate between wobbling and monotonic instabilities as the orbital radius is increased progressively, with the envelope of the monotonic instabilities arising at a memory lower than that of wobbling instabilities (figure 3).

4. Physical interpretations of the wobbling and monotonic instability tongues

Having established concise asymptotic formulae describing the onset of wobbling and monotonic instabilities, we now deepen our physical understanding by comparing the efficacy of different heuristic arguments for the critical radii at the onset of instability. Specifically, we first compare the predictions of several energy-based heuristics suggested in prior investigations to those of our numerical and asymptotic results (§ 4.1). We then propose a new heuristic based on the form of the mean pilot wave (§ 4.2), which we show to be more fruitful than prior heuristics.

4.1. Energy-like heuristics

The hydrodynamic pilot-wave system is a driven-dissipative system: energy is supplied by the system vibration and ultimately lost through viscous dissipation. Nevertheless, quasi-steady and periodic dynamical states arise in which the energy input precisely balances that lost through dissipation, and energy is exchanged primarily between the bouncing drop and the Faraday wave field excited by its impact (Moláček & Bush 2013*a*,*b*). For inviscid gravity-capillary waves, kinetic energy is exchanged with gravitational potential and surface energies. For our investigation, it thus suffices to characterise the system energetics in terms of the wave energy, which is computed readily from our model.

Owing to the slow spatial decay of the walker wave field (2.1b), the standard wave energy integral diverges when integrating over the plane. Instead, we adopt the notion of wave intensity E, as coined by Hubert $et\ al.\ (2022)$, which acts as a suitable proxy for the sum of the wave field gravitational potential and surface energies. In dimensional units,

we thus define

$$E = \lim_{R \to \infty} \frac{1}{R} \left[\int_{|x| < R} \frac{1}{2} \rho g h^2 \, \mathrm{d}x + \int_{|x| < R} \sigma \left(\sqrt{1 + |\nabla h|^2} - 1 \right) \, \mathrm{d}x \right], \tag{4.1}$$

where σ and ρ are the fluid surface tension coefficient and density, respectively, and E has units of energy per unit length. For small wave slope, we henceforth approximate the bracketed term in the second integral by $\frac{1}{2}|\nabla h|^2$ (see Appendix E). By applying the divergence theorem to the surface energy contribution and exploiting the fact that the wave field is monochromatic with wavenumber k_F , we demonstrate in § E.1 that the contributions from gravitational and surface energies are proportional to each other, and (4.1) reduces to

$$E = (\rho g + \sigma k_F^2) \lim_{R \to \infty} \frac{1}{2R} \int_{|x| \le R} h^2(x, t) \, \mathrm{d}x, \tag{4.2}$$

an expression proportional to that obtained by Labousse *et al.* (2016*b*) and Hubert *et al.* (2022), who neglected the contribution of surface tension.

To analyse the wave intensity, we transform (4.2) to dimensionless variables by defining $\hat{h} = h/h_0$ and $\hat{E} = E/E_0$, where $h_0 = AT_W/T_F$ and $E_0 = h_0^2 k_F^{-1} (\rho g + \sigma k_F^2)$ are the characteristic wave height and intensity. By once again taking k_F^{-1} and T_W as the units of length and time (see § 2.1), we define the dimensionless wave intensity by

$$\hat{E} = \lim_{R \to \infty} \frac{1}{2R} \int_{|\mathbf{x}| < R} \hat{h}^2(\mathbf{x}, t) \, d\mathbf{x}, \tag{4.3}$$

where

$$\hat{h}(x,t) = \int_{-\infty}^{t} J_0(|x - x_p(s)|) e^{-\mu(t-s)} ds$$
 (4.4)

is the dimensionless form of the pilot wave.

For circular orbital motion, the dimensionless wave intensity takes the remarkably simple form (see § E.2)

$$\hat{E} = \frac{1}{\mu} \mathcal{I}_0(0), \tag{4.5}$$

where $\mathcal{I}_0(0)$ (defined in (2.7*a*)) is the amplitude of the wave field beneath the droplet (Durey & Bush 2021). Since the wave intensity and droplet gravitational potential energy are proportional to each other for orbital motion, either quantity serves equally well as a diagnostic measure of orbital stability. We may now use the tangential force balance (2.13) to deduce that the orbital wave intensity (4.5) reduces to

$$\hat{E} = \frac{1}{\mu^2} \left(1 - \frac{U^2}{2} \right),\tag{4.6}$$

where $U = r_0 \omega$ is the orbital speed. For fixed wave decay rate μ , we conclude that the wave intensity is smaller for faster orbiters. Moreover, the transition from stationary bouncing (U = 0) to orbiting (U > 0) serves to decrease the wave energy, as does the transition from bouncing to rectilinear walking (Durey & Milewski 2017). Finally, combining the bound $\hat{E} > 0$ with (4.6) supplies the upper bound on the orbital speed noted in § 2.2, namely $U < \sqrt{2}$

To explore the connection between wave intensity (or, equivalently, droplet gravitational potential energy) and orbital stability, we present the dependence of the wave intensity on

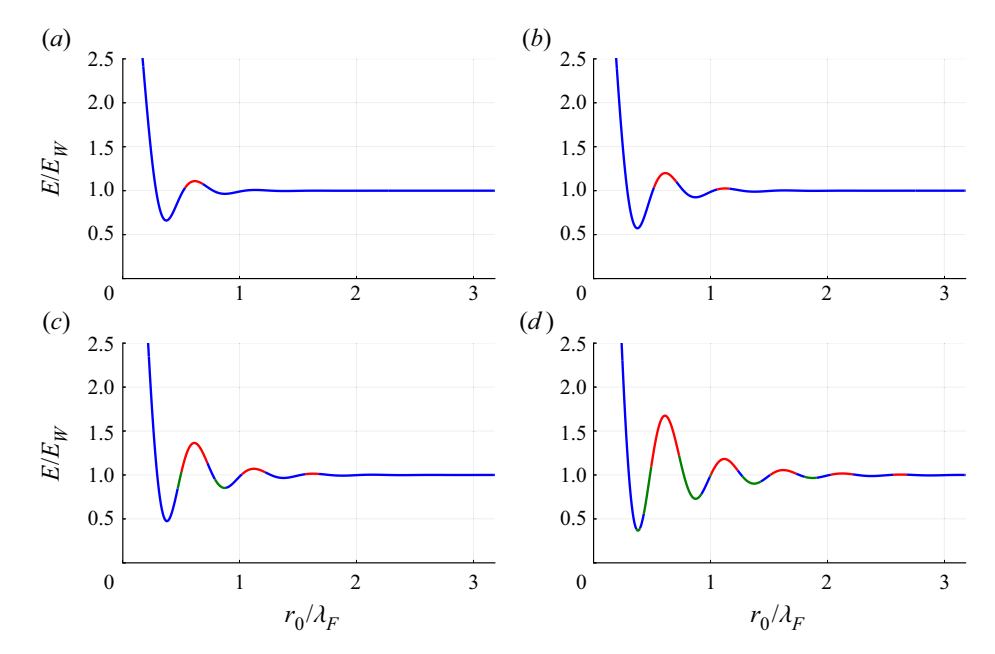


Figure 6. The dependence of the wave intensity E (see (4.6)), relative to that of a walker, E_W , on the orbital radius for $\kappa_0 = 1.6$ and Γ values (a) 0.7, (b) 0.75, (c) 0.8, and (d) 0.85. The colour scheme is the same as in figure 2. The onsets of monotonic and wobbling instabilities are correlated with, respectively, the local maxima and minima of the wave intensity E.

the orbital radius in figure 6. As the wave decay rate μ is decreased, we observe that all monotonic instabilities arise in the vicinity of radii that maximise the wave intensity, while wobbling instabilities generally arise close to the orbital radii that minimise the wave intensity. (We note that the other wobbling instabilities appear as side bands to the first monotonic instability tongue; see figure 2(b).) This correlation is thus indicative of an underlying orbital energy principle, according to which the magnitude of the wave intensity prescribes the stability of the corresponding circular orbit (Durey 2018). To test this hypothesis, we present in figure 7 the orbital radius arising at the tip of each of the first four wobbling (green curves) and monotonic (red curves) instability tongues, i.e. the radii that locally minimise Γ along the stability boundary (the white curve in figure 2b). For each critical value of Γ (or $\mu = 1 - \Gamma$), we compare the corresponding critical orbital radius to the extrema of the wave field intensity (blue curves), confirming our observation that maxima and minima of E correspond approximately to the tips of the monotonic and wobbling instability tongues, respectively, with the agreement improving for larger orbital radius.

To further assess the utility of different energy-based heuristics, we also compare the critical radii to the zeros of $J_0(r_0)$, $J_1(r_0)$ and $J_2(r_0)$, as suggested by Labousse *et al.* (2016*a*). As presented in figure 7, the monotonic instabilities appear at radii slightly smaller than the zeros of $J_1(r_0)$, while the wobbling instabilities typically align closely with the zeros of $J_2(r_0)$. We note, however, that the critical radii exhibit a weak dependence on κ_0 that is not captured by the zeros of Bessel functions. On the other hand, the zeros of $J_1(r_0)$ approach the radii satisfying $\sin(2r_0) = 1$ for larger orbital radius, consistent with our asymptotic analysis of the monotonic instability (§ 3.2). Likewise, the zeros of $J_0(r_0)$ and $J_2(r_0)$ both approach the radii satisfying $\sin(2r_0) = -1$, in agreement with our

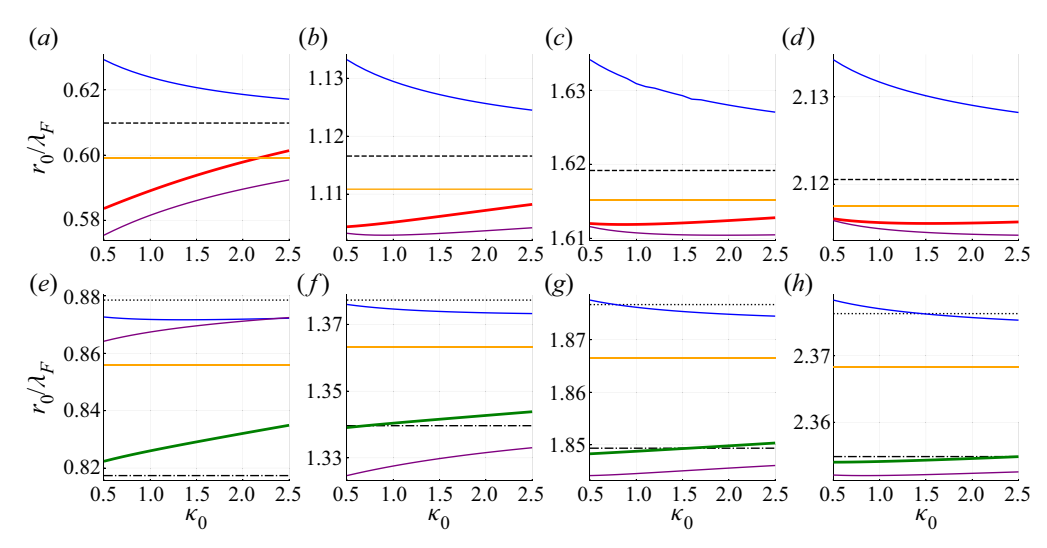


Figure 7. The dependence of the critical orbital radius on the inertia-to-drag ratio, $\kappa_0 = m/DT_W$, for (a-d) monotonic (red) and (e-h) wobbling (green) instabilities. Each plot corresponds to a different instability tongue in figure 2(b), with radius increasing from left to right. We compare the critical radii of monotonic and wobbling instabilities to those that maximise and minimise the wave intensity ((4.5), blue) and the derivative of the mean wave force (orange, § 4.2), respectively. We also compare the critical radii with those predicted by the asymptotic formulae for monotonic ((3.8) and (3.12)) and wobbling ((3.9) and (3.10a,b)) instabilities (purple). The black horizontal lines correspond to zeros of $J_0(k_F r_0)$ (dotted), $J_1(k_F r_0)$ (dashed) and $J_2(k_F r_0)$ (dot-dashed), whose relation to orbital stability was noted by Labousse *et al.* (2016a). With increasing orbital radius, the range of each vertical axis narrows, reflecting the improved prediction of each heuristic.

analysis of wobbling instabilities (§ 3.2). We thus rationalise the Labousse *et al.* (2016*a*) conjecture that the zeros of Bessel functions are likely to identify the loci of the most unstable orbital radii.

Finally, we compare the critical orbital radii of the numerically computed stability boundary with our asymptotic formulae derived in §§ 3.2 and 3.3. Specifically, we minimise numerically the first-order solutions, corresponding to the combination of (3.8) and (3.12) for the monotonic instability tongues (figures 7a-d), and (3.9) and (3.10a,b) for the wobbling instability tongues (figures 7e-h). Our asymptotic results appear as purple curves in figure 7, and agree favourably with the critical radii of the numerical stability boundary, generally capturing the correct trend with increasing κ_0 , and satisfying the anticipated $O(r_0^{-2})$ convergence as the orbital radius is increased. One limitation of this approach, however, is the absence of a local minimum for the first wobbling tongue when using the first-order correction (3.10a,b) (owing to the parasitic influence of the cot($2r_0$) term). Instead, we compare the critical radius in this case to that computed from the leading-order solution given in (3.9), which explains the larger discrepancy in figure 7(e). Nevertheless, our large-radius asymptotic results work surprisingly well in this case, where the orbital radius is relatively small.

In summary, we find that the simple heuristic criteria for the critical orbital radii are moderately successful, with the agreement improving for larger orbital radius. The zeros of Bessel functions generally give better agreement with the numerical results than the extrema of the wave intensity, or, equivalently, the droplet's gravitational potential energy. Notably, incorporating the droplet's kinetic energy within this latter heuristic does not affect the critical orbital radii significantly, with the resultant curves generally being

indistinguishable from the blue curves in figure 7. Finally, these heuristic arguments are limited by their inability to predict the critical memory at the onset of instability and to capture the dependence of the critical radii on κ_0 . Both quantities may be computed accurately using our asymptotic framework.

4.2. The mean wave field

Although the zeros of $J_1(r_0)$ and $J_2(r_0)$ provide satisfactory agreement with the numerical results for the tip of each instability tongue (Labousse *et al.* 2016*a*), this heuristic does not provide a rationale for the type of instability. We proceed to develop a new dynamic rationale that is asymptotically equivalent to the heuristic of Labousse *et al.* (2016*a*), yet explains the alternation between monotonic and wobbling instabilities with increasing orbital radius evident in figure 2(b).

We proceed by developing a dynamical interpretation of orbital instability in terms of the force applied by the mean wave field, specifically that averaged over one orbital period. One may decompose the orbital wave field into a continually evolving, non-axisymmetric component that serves to propel the droplet at a constant horizontal speed (Bush, Oza & Moláček 2014; Labousse & Perrard 2014), and a static axisymmetric component (the mean wave field) that imparts either an inward or outward radial force to the droplet (Labousse *et al.* 2014; Durey *et al.* 2018). We note that a similar decomposition of the wave field applies when considering small perturbations from orbital motion, for which the mean wave field may now be regarded as a quasi-static potential. Notably, Perrard *et al.* (2014*b*) used this potential to determine the radii of quantised circular orbits; in contrast, we use this potential to explain the onset of orbital instability.

The dimensionless axisymmetric mean wave field h(r) accompanying a droplet executing a circular orbit of radius r_0 about the origin is given by (Perrard *et al.* 2014*b*; Tambasco & Bush 2018)

$$\bar{h}(r) = \frac{1}{\mu} J_0(r_0) J_0(r).$$
 (4.7)

We thus deduce that the dimensionless radial wave force

$$\mathcal{F}(r_0) = -2 \left. \frac{\mathrm{d}\bar{h}}{\mathrm{d}r} \right|_{r=r_0} \tag{4.8}$$

applied by the mean wave field along the droplet's trajectory is

$$\mathcal{F}(r_0) = \frac{2}{\mu} J_0(r_0) J_1(r_0) = -\frac{2\cos(2r_0)}{\mu \pi r_0} + O\left(\frac{1}{r_0^2}\right), \tag{4.9}$$

with derivative

$$\mathcal{F}'(r_0) = \frac{4\sin(2r_0)}{\mu\pi r_0} + O\left(\frac{1}{r_0^2}\right). \tag{4.10}$$

As shown in § 3.1, wobbling instabilities occur when $\sin(2r_0) < 0$, whereas monotonic instabilities occur when $\sin(2r_0) > 0$. Equation (4.10) suggests that for sufficiently large r_0 , the type of instability exhibited by increasing the memory at constant r_0 is thus related to the derivative of the mean wave force. Specifically, if $\mathcal{F}'(r_0) < 0$, then the corresponding circular orbit destabilises via a wobbling instability. Conversely, if $\mathcal{F}'(r_0) > 0$, then the circular orbit destabilises via a monotonic instability.

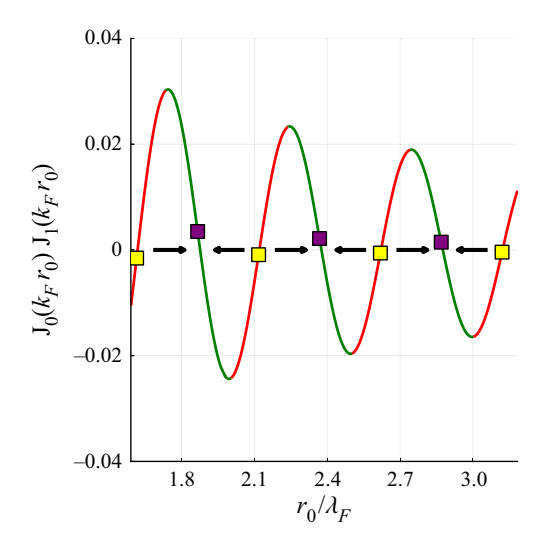


Figure 8. Schematic representation of orbital instability in terms of the mean wave force. We present the dependence of $\frac{1}{2}\mu \mathcal{F}(r_0) = J_0(k_F r_0) J_1(k_F r_0)$, which is proportional to the mean wave force, on the orbital radius for $\kappa_0 = 1.6$. The curve is colour-coded according to the type of instability arising along the stability boundary (white curve in figure 2b). Along green and red portions of the curve, the mean wave field acts like an attractive and repulsive spring, respectively, giving rise to wobbling and monotonic instabilities. The sign of the mean wave force is denoted by arrows, and its slope is maximised and minimised at the yellow and purple squares, respectively.

This correlation between the sign of $\mathcal{F}'(r_0)$ and the form of instability can be interpreted physically through consideration of figure 8. As in our linear stability analysis (§ 2.3), we posit that the instantaneous orbital radius $r_p(t)$ has the form $r_p(t) = r_0 + \epsilon r_1(t)$, where $0 < \epsilon \ll 1$ is a small parameter, and $r_1(t)$ denotes the perturbation to the orbital radius. It follows that the force exerted by the mean wave field may be approximated by $\mathcal{F}(r_n) \approx \mathcal{F}(r_0) + \epsilon r_1 \mathcal{F}'(r_0)$; thus the direction and magnitude of the perturbed wave force is prescribed by $\mathcal{F}'(r_0)$. When $\mathcal{F}'(r_0) > 0$, an outward radial perturbation $(r_1 > 0)$ results in an increase in the outward force that drives the droplet away from equilibrium. Similarly, an inward perturbation $(r_1 < 0)$ decreases the outward force. When $\mathcal{F}'(r_0) > 0$, we may thus regard the mean wave force as a repulsive spring force that induces monotonic changes in the orbital radius. Conversely, when $\mathcal{F}'(r_0) < 0$, the mean wave force behaves like an attractive spring that opposes any perturbations in the orbital radius from r_0 and so induces oscillations in the orbital radius. This physical picture is consistent with the observation that the type of instability changes when $\mathcal{F}'(r_0)$ changes sign (see figure 8). Moreover, the mean wave field's opposition to perturbations from r_0 hinders the onset of the corresponding wobbling instabilities, which is consistent with wobbling instabilities occurring at higher memory than their monotonic counterparts. Finally, the magnitude of the radial wave force increases as μ decreases, thereby increasing the sensitivity to perturbation at higher memory.

In an attempt to rationalise the radii of the most unstable circular orbits (corresponding to the tips of the stability tongues in figure 2b), we follow the above argument and posit that these will correspond to the radii marked by the largest relative change in the perturbation force, as characterised by the coefficient $\mathcal{F}'(r_0)$. The coefficient $\mathcal{F}'(r_0)$ is maximised in magnitude at critical radii r_c satisfying $\mathcal{F}''(r_c) = 0$. Specifically, maxima in $\mathcal{F}'(r_0)$ correspond to monotonic instabilities, and minima in $\mathcal{F}'(r_0)$ correspond to

wobbling instabilities. In figure 7, we observe that the most unstable radii predicted by this heuristic ($\mathcal{F}''(r_c) = 0$) exhibit excellent quantitative agreement with the numerical solution for monotonic instabilities, and a favourable agreement for wobbling instabilities. The limitation of this heuristic for wobbling instabilities is presumably rooted in small deviations of the mean wave field from a quasi-static potential for oscillatory droplet motion

In summary, we have developed a new rationale for the onset of wobbling and monotonic instabilities in terms of the force exerted on the droplet by the mean wave field. Specifically, our investigation indicates that the critical radii r_c at the onset of instability approximately satisfy $\mathcal{F}''(r_c) = 0$. In contrast to the heuristic arguments presented in §4.1, our rationale explains the alternation of wobbling and monotonic instabilities with increasing orbital radius. Moreover, our study suggests that the oscillatory and quasi-periodic nature of the stability boundary (see figure 2b) is correlated with the quasi-monochromatic mean wave field. As a caveat, our rationale is valid only for circular orbits near the stability boundary, and so cannot be used to differentiate between stable and unstable orbits. Like the heuristic arguments presented in §4.1, our rationale neither predicts the critical memory of instability nor accounts for the dependence on the parameter κ_0 . Nevertheless, it performs remarkably well over the range of values of the inertia-to-drag parameter κ_0 accessible in the laboratory.

5. Discussion

We have examined the stability of circular inertial orbits executed by droplets walking in a rotating frame. We have developed an asymptotic framework for studying orbital stability, specifically for characterising the critical memory at the onset of the wobbling and monotonic instabilities. Our asymptotic model rationalises the repeating structure of the stability diagram in figure 2, which we demonstrate to be rooted in the periodic nature of the mean wave field. Our theory not only rationalises the preponderance of 2-wobble instabilities, but also predicts that the destabilisation frequency is exactly twice the angular frequency at the most unstable orbital radii, corresponding to the tips of the stability tongues. In rationalising the most unstable wobbling frequencies reported in the experiments of Harris & Bush (2014) and simulations of Oza *et al.* (2014*b*), our study has demonstrated the importance of resonant instability in orbital pilot-wave dynamics.

Our asymptotic results show that orbital instability is enhanced through resonance. Resonant instabilities have been reported in other pilot-wave systems, including the in-line speed oscillations of the free walker (Bacot *et al.* 2019; Durey *et al.* 2020*b*), 4ω orbital instabilities in a linear central force (Kurianski, Oza & Bush 2017), and 2ω , 3ω and 4ω instabilities for pairs of orbiting droplets (Oza *et al.* 2017; Durey 2018). This naturally raises the question of the prevalence of resonant instabilities in other pilot-wave systems. In subsequent work, we will consider the more complex orbits arising for a droplet in a linear central force, where richer resonances are expected to arise. We expect the asymptotic framework developed here to be well-suited to addressing this class of problems.

It is worth enumerating the limitations of our study. In our study, we have assumed resonant bouncing at constant bouncing phase, and neglected the far-field exponential decay of the wave field (Moláček & Bush 2013b; Turton, Couchman & Bush 2018; Tadrist et al. 2018). Both of these approximations are known to break down for multi-droplet systems (Oza et al. 2017; Arbelaiz, Oza & Bush 2018; Galeano-Rios et al. 2018; Couchman, Turton & Bush 2019), and so might become significant at sufficiently high orbital memory. In addition, we have restricted our attention to the linear stability of circular orbits, and so not considered nonlinear effects such as the jump up/down

instabilities reported by Harris & Bush (2014) and Oza *et al.* (2014*b*). Finally, we have not considered instability in the large-radius limit inaccessible in the laboratory, which one expects to be related to the instability of the free, rectilinear walking state (Bacot *et al.* 2019; Hubert *et al.* 2019; Durey *et al.* 2020*b*), a matter to be considered elsewhere.

We have also compared the success of various heuristics for predicting the onset of orbital instability in our system. Our study has lead us to introduce two new heuristics, specifically the wave intensity and the mean wave force. We show that the orbital radii corresponding to the onset of monotonic and wobbling instabilities generally arise near the radii that maximise and minimise the wave intensity, respectively. We have also demonstrated the equivalence of the wave intensity and wave height beneath the drop as proxies for the droplet energy; specifically, the wave energy is proportional to the gravitational potential energy of the drop. This result provides new insight into the observations made by Couchman & Bush (2020) and Thomson *et al.* (2020) that a ring of droplets rearranges itself so as to minimise the mean gravitational potential of the droplets, suggesting that they are doing so in order to minimise the global wave energy.

Labousse *et al.* (2016*a*) proposed that wobbling and monotonic instabilities arise from orbits that receive little wave energy from the J₁ and J₂ modes, and postulated that the most unstable orbital radii occur at zeros of these Bessel functions. We have demonstrated that this heuristic leads to impressive agreement with our numerical calculations over a wide range of parameter values, and outperforms our wave intensity extremisation principle, defined in § 4.1. However, the Labousse *et al.* (2016*a*) heuristic does not provide a physical mechanism that distinguishes between the wobbling and monotonic instabilities. Our new heuristic based on the form of the mean wave field (§ 4.2) indicates the correlation between the type of instability and the derivative of the mean wave force, and so sheds light on the alternation between wobbling and monotonic instabilities with increasing orbital radius. The general utility of mean-pilot-wave-based heuristics will be considered elsewhere.

Acknowledgements. The authors thank A. Oza and D. Harris for providing the images presented in figure 1 and the data presented in figure 4.

Funding. We gratefully acknowledge the generous financial support of the NSF through grant CMMI-2154151.

Declaration of interests. The authors report no conflict of interest.

Data availability statement. The data that support the findings of this study are available from the corresponding author, J.W.M.B., upon reasonable request.

Author ORCIDs.

- Nicholas Liu https://orcid.org/0000-0002-8962-8536;
- Matthew Durey https://orcid.org/0000-0002-4232-1705;
- John W.M. Bush https://orcid.org/0000-0002-7936-7256.

Author contributions. J.W.M.B. and M.D. conceived the project. N.L. was responsible for the mathematical and numerical developments, which were overseen by M.D. All authors contributed to the writing.

Appendix A. Physical parameters

We here define the Faraday wavenumber k_F , drag factor D, and wave amplitude parameter A, in terms of physical quantities (Oza *et al.* 2013, 2014*a*). Specifically, the Faraday wavenumber satisfies the gravity-capillary dispersion relation (Benjamin & Ursell 1954)

$$(\pi f)^2 = \left(gk_F + \frac{\sigma k_F^3}{\rho}\right) \tanh(k_F H),\tag{A1}$$

where σ is the coefficient of surface tension, ρ is the fluid density, and H is the fluid depth. Furthermore, we define the drag factor

$$D = 0.17 \, mg \sqrt{\frac{\rho R_D}{\sigma}} + 6\pi \mu_{air} R_D \left(1 + \frac{\rho_{air} g R_D}{12 \mu_{air} f} \right), \tag{A2}$$

and wave amplitude

$$A = \frac{1}{\sqrt{2\pi}} \frac{k_F R_D}{3k_F^2 R_D^2 + Bo} \frac{R_D k_F^2 v_{eff}^{1/2}}{\sigma \sqrt{T_F}} mg T_F \sin \Phi, \tag{A3}$$

where R_D is the droplet radius, μ_{air} and ρ_{air} are the dynamic viscosity and density of air, respectively, ν_{eff} is the effective fluid kinematic viscosity (Moláček & Bush 2013b), $Bo = \rho g R_D^2 / \sigma$ is the Bond number, and $\sin \Phi = 0.2$ is the droplet impact phase (Oza *et al.* 2013, 2014b).

Appendix B. Evaluation of stability integrals

We proceed to evaluate analytically the stability integrals defined in (2.7), where we leverage the relationship between the stability integrals (2.9a,b) to evaluate S_m and C_m in terms of I_m only. The evaluation of each stability integral hinges on the observation that $I_{2m}(2r_0 \sin(x))$ is even and π -periodic, and so may be expressed in terms of its bi-infinite cosine series (derived from Gradshteyn & Ryzhik (2014, § 6.681)) as

$$J_{2m}(2r_0\sin(x)) = \sum_{n=-\infty}^{\infty} (-1)^n J_{m+n}(r_0) J_{m-n}(r_0) \cos(2nx).$$
 (B1)

By performing the change of integration variable $t \mapsto \omega t$ in (2.7a) and using the cosine series expansion (B1), the integral $\mathcal{I}_m(s)$ may be recast as the infinite sum

$$\mathcal{I}_{m}(s) = \frac{1}{\omega} \sum_{n=-\infty}^{\infty} (-1)^{n} J_{m+n}(r_{0}) J_{m-n}(r_{0}) \int_{0}^{\infty} \cos(nt) e^{-\eta t} dt,$$
 (B2)

where $\eta = (\mu + s)/\omega$ and $\text{Re}(\eta) > 0$. By integrating each of the resultant integrals analytically, we deduce that the stability integral is equivalent to

$$\mathcal{I}_{m}(s) = \frac{\eta}{\omega} \sum_{n=-\infty}^{\infty} \frac{(-1)^{n} J_{m+n}(r_{0}) J_{m-n}(r_{0})}{\eta^{2} + n^{2}}.$$
 (B3)

This formulation is convenient for numerical computation of the stability integrals, and is used in the construction of orbital stability diagrams and the tracking of orbital stability boundaries (e.g. figure 2). However, further analytical progress can be made by using a partial fraction expansion in (B3) and applying the Lerche–Newberger sum rule (Newberger 1982; Bakker & Temme 1984), giving rise to the closed-form expression given in (2.8), which forms the basis of our analytical developments.

Notably, the sum (or difference) appearing in the Bessel function orders in (2.8) when m = 1 complicates the application of large-argument asymptotic expansions in our study. As such, we derive two Bessel function identities that assist with the elimination of the sum in the order, thereby allowing us to derive a set of convenient equations for further

analysis. To proceed, we first recall the Bessel function Wronskian, recurrence relation and derivative expression given by (Abramowitz & Stegun 1948)

$$J_{\nu}(x)J_{1-\nu}(x) + J_{-\nu}(x)J_{\nu-1}(x) = \frac{2\sin(\nu\pi)}{\pi x},$$
 (B4a)

$$J_{\nu-1}(x) + J_{\nu+1}(x) = \frac{2\nu}{x} J_{\nu}(x), \tag{B4b}$$

$$J_{\nu-1}(x) - J_{\nu+1}(x) = 2J'_{\nu}(x), \tag{B4c}$$

respectively, which form the basis of our forthcoming algebraic manipulations. To derive the first identity, we apply the recurrence relation (B4b), add and subtract $(2\nu/x) J_{-\nu}(x) J_{\nu-1}(x)$ to and from the resultant expression, and simplify using the Wronskian (B4a) and derivative relation (B4c) to obtain

$$J_{1-\nu}(x)J_{-1+\nu}(x) - J_{1+\nu}(x)J_{-1-\nu}(x) = \frac{4\nu\sin(\nu\pi)}{\pi x^2} - \frac{4\nu}{x}J_{-\nu}(x)J_{\nu}'(x).$$
 (B5)

To derive the second identity, we differentiate the Wronskian identity (B4a) and apply the recurrence relation (B4b) to find that

$$J_{1-\nu}(x)J_{\nu}'(x) + J_{1+\nu}(x)J_{-\nu}'(x) = -2J_{-\nu}'(x)J_{\nu}'(x) - \frac{2\nu\sin(\pi\nu)}{\pi x^2}.$$
 (B6)

We now use the relations (B5) and (B6) in conjunction with (2.8) and (2.9a,b) to evaluate the integrals and integral combinations arising in the stability problem (2.6), yielding

$$\mathcal{I}_0(0) = \frac{\pi \operatorname{csch}(\pi \beta)}{\omega} \operatorname{J}_{i\beta}(r_0) \operatorname{J}_{-i\beta}(r_0), \tag{B7a}$$

$$\frac{\partial \mathcal{I}_0(0)}{\partial r_0} = \frac{-2\pi \operatorname{csch}(\pi\beta)}{\omega} \left(\frac{\mathrm{i} \sinh(\pi\beta)}{\pi r_0} - J_{-\mathrm{i}\beta}(r_0) J'_{\mathrm{i}\beta}(r_0) \right),\tag{B7b}$$

$$S_0(s) = \frac{2\pi\eta \operatorname{csch}(\pi\eta)}{\omega} \left(\frac{\mathrm{i}\sinh(\pi\eta)}{\pi r_0^2} - \frac{\mathrm{J}_{-\mathrm{i}\eta}(r_0)\,\mathrm{J}'_{\mathrm{i}\eta}(r_0)}{r_0} \right),\tag{B7c}$$

$$C_0(s) - \mathcal{I}_1(s) = -\frac{2\mathrm{i}\eta\pi \operatorname{csch}(\pi\eta)}{r_0^2\omega} \left(\frac{\mathrm{i}\sinh(\pi\eta)}{\pi} - \mathrm{i}\eta\operatorname{J}_{\mathrm{i}\eta}(r_0)\operatorname{J}_{-\mathrm{i}\eta}(r_0)\right), \tag{B7d}$$

$$C_0(s) + \mathcal{I}_1(s) = \frac{2\pi \operatorname{csch}(\pi \eta)}{\omega} \left(\frac{\eta \sinh(\pi \eta)}{\pi r_0^2} + J'_{i\eta}(r_0) J'_{-i\eta}(r_0) \right), \tag{B7e}$$

where we recall that $\eta = (\mu + s)/\omega$, and $\beta = \mu/\omega$ is the reciprocal of the orbital memory.

Appendix C. Stationary phase point contributions to stability integrals

We seek the contributions at each critical point to the integral $\mathcal{L}_m(\xi)$, defined in (2.15), for which we consider $r_0 \gg 1$ and $\xi = O(1)$. We first consider the contribution to $\mathcal{L}_m(\xi)$ near the edges of the integration region, namely $\theta = 0$ and $\theta = 2\pi$, which we denote by $\mathcal{L}_{m,0}(\xi)$ and $\mathcal{L}_{m,2\pi}(\xi)$, respectively. To determine $\mathcal{L}_{m,0}(\xi)$, we approximate $\sin(\theta/2) \approx \theta/2$ in the argument of the Bessel function, and recast the integration region as

$$\mathcal{L}_{m,0}(\xi) = \int_0^\infty J_{2m}(r_0\theta) e^{-(\beta+i\xi)\theta} d\theta - \int_{2\pi}^\infty J_{2m}(r_0\theta) e^{-(\beta+i\xi)\theta} d\theta.$$
 (C1)

The first integral may be evaluated analytically (Abramowitz & Stegun 1948), and it remains now to estimate the size of the second integral. We approximate the integrand

by utilising the large-argument Bessel function expansion (Abramowitz & Stegun 1948) and noting that $\theta \ge 2\pi$ across the integration domain; then, by evaluating the resultant integral analytically, we obtain the approximate bound

$$\int_{2\pi}^{\infty} J_{2m}(r_0\theta) e^{-(\beta+i\xi)\theta} d\theta \sim \sqrt{\frac{1}{\pi^2 r_0}} \int_{2\pi}^{\infty} \cos(r_0\theta - \varphi_m) e^{-(\beta+i\xi)\theta} d\theta = O\left(\frac{e^{-2\pi\beta}}{r_0\sqrt{r_0}}\right),$$
(C2)

where $\varphi_m = \frac{1}{4}\pi(1+4m)$ is a constant phase shift. Provided that β is of size at most $O(r_0)$, the analytical evaluation of the first integral in (C1) determines that this term is the dominant contribution to $\mathcal{L}_{m,0}$. By neglecting the contribution from the second integral in (C1), we deduce that $\mathcal{L}_{m,0} = O(r_0^{-1})$. The periodicity of the non-exponential portion of the integrand indicates that the contribution near $\theta = 2\pi$ satisfies $\mathcal{L}_{m,2\pi}(\xi) = \mathcal{L}_{m,0}(\xi) e^{-2\pi(\beta+i\xi)}$. The factor $e^{-2\pi\beta}$ ensures that the contribution $\mathcal{L}_{m,2\pi}(\xi)$ is negligible relative to $\mathcal{L}_{m,0}(\xi)$ and may henceforth be neglected.

We now determine the contributions arising near points of stationary phase. The internal contribution is localised about $\theta = \pi$, and we denote this contribution by $\mathcal{L}_{m,\pi}(\xi)$. To proceed, we deform the integration region to a small region about $\theta = \pi$, namely $\pi - \delta < \theta < \pi + \delta$ with $0 < \delta \ll 1$, and define

$$\mathcal{L}_{m,\pi}(\xi) = \int_{\pi-\delta}^{\pi+\delta} J_{2m}\left(2r_0 \sin\left(\frac{\theta}{2}\right)\right) e^{-(\beta+i\xi)\theta} d\theta.$$
 (C3)

By applying the large-argument expansion for the Bessel function (Abramowitz & Stegun 1948) and utilising the Taylor expansion $\sin(\theta/2) \approx 1 - \frac{1}{8}(\theta - \pi)^2$, we determine the approximation

$$\mathcal{L}_{m,\pi}(\xi) \sim \frac{e^{-(\beta + i\xi)\pi}}{2\sqrt{\pi r_0}} \sum_{+} e^{\pm i\varphi_m} \int_{\pi-\delta}^{\pi+\delta} e^{\mp i2r_0 \left(1 - \frac{1}{8}(\theta - \pi)^2\right)} d\theta.$$
 (C4)

The leading-order form of the resultant integral may be determined using method of stationary phase for $r_0 \gg 1$, giving rise to the contribution

$$\mathcal{L}_{m,\pi}(\xi) \sim -\frac{2e^{-\pi(\beta+i\xi)}}{r_0}\cos(2r_0 + \varphi_m).$$
 (C5)

Appendix D. Asymptotic expansions for the wobbling regime

Along stability boundaries (with $s = i\xi\omega$), the stability integrals (2.7) are all evaluated in terms of Bessel functions of complex order $\pm i\zeta$ and real argument r_0 , where $\zeta \in \{\beta, \beta + i\xi\}$ (see (B7)). For wobbling and monotonic instabilities, corresponding to $\beta = O(\ln(r_0))$ and $\xi = O(1)$, the order of the Bessel function is much smaller than the argument. Thus we may expand each of the Bessel function products in (B7) by applying the large-argument asymptotic expansion to each Bessel function (Abramowitz & Stegun

1948). Direct evaluation by Mathematica yields

$$J_{-i\zeta}(r_0) J'_{i\zeta}(r_0) = \frac{\cos(2r_0) + i\sinh(\xi\pi)}{\pi r_0} - \frac{\cosh(\xi\pi)}{2\pi r_0^2} + \frac{(4\xi^2 - 1)\sin(2r_0)}{4\pi r_0^2} + \frac{3(1 + 4\xi^2)\cosh(\xi\pi)}{16\pi r_0^4} + O\left(\frac{1}{r_0^3}\right), \qquad (D1a)$$

$$J_{i\zeta}(r_0) J_{-i\zeta}(r_0) = \frac{\sin(2r_0) + \cosh(\xi\pi)}{\pi r_0} - \frac{1 + 4\xi^2}{4\pi r_0^2} \left(\frac{\cosh(\xi\pi)}{2r_0} + \cos(2r_0)\right) + O\left(\frac{1}{r_0^3}\right), \qquad (D1b)$$

$$J'_{i\zeta}(r_0) J'_{-i\zeta}(r_0) = \frac{-\sin(2r_0) + \cosh(\zeta \pi)}{\pi r_0} + \frac{(3 + 4\zeta^2) \cosh(\zeta \pi)}{8\pi r_0^3} + \frac{(-3 + 4\zeta^2) \cos(2r_0)}{4\pi r_0^2} + O\left(\frac{1}{r_0^3}\right),$$
(D1c)

where all terms necessary for the dominant balance $e^{\pi\beta} = O(r_0^2)$ have been retained, and the expansions (D1) are valid when $|\zeta^2 + \frac{1}{4}| \ll r_0$ (Abramowitz & Stegun 1948). By substituting these expansions into the analytical expressions for each of the stability integrals (see (B7)), we deduce that the stability coefficients (see (2.12)) have the asymptotic form

$$\mathcal{A} = -\frac{2\sin(2r_0)}{U} \left(\operatorname{csch}(\pi(\beta + i\xi)) + \operatorname{csch}(\pi\beta) \right) + \frac{(4\beta^2 - 7)\cos(2r_0)\operatorname{csch}(\pi\beta)}{2Ur_0} + \frac{3 - \xi^2}{Ur_0^2} - \frac{\kappa_0 \xi^2 U^2}{r_0^2} + \frac{\cos(2r_0)\operatorname{csch}(\pi(\beta + i\xi))(-3 + 4\beta^2 + 8i\beta\xi - 4\xi^2)}{2Ur_0} + O\left(\frac{1}{r_0^4}\right), \tag{D2}a$$

$$\mathcal{B} = \frac{\mathrm{i} \kappa_0 \xi \, U^2}{r_0^2} - \frac{2\mathrm{i} \xi}{U r_0^2} + \frac{2 \cos(2r_0)}{U r_0} \Big(\mathrm{csch}(\pi \beta) \, (\mathrm{i} \xi - \beta)$$

$$+\operatorname{csch}(\pi(\beta+\mathrm{i}\xi))(\beta+\mathrm{i}\xi)) + O\left(\frac{1}{r_0^4}\right),\tag{D2b}$$

$$\mathscr{C} = \frac{2U}{r_0} - \frac{2(\beta + i\xi)}{Ur_0^2} + \frac{i\kappa_0\xi U^2}{r_0^2} + O\left(\frac{1}{r_0^3}\right),\tag{D2c}$$

$$\mathscr{D} = \frac{2\mathrm{i}\xi U}{r_0} - \frac{2\mathrm{i}\xi(\beta + \mathrm{i}\xi)}{Ur_0^2} - \frac{\kappa_0 \xi^2 U^2}{r_0^2} + O\left(\frac{1}{r_0^3}\right),\tag{D2d}$$

where we have again utilised the dominant balance $e^{\pi\beta} = O(r_0^2)$.

Appendix E. Wave intensity

E.1. Surface energy contribution

We proceed to show that the contribution of surface energy to the wave intensity is proportional to that of gravitational potential energy. For small wave slopes, we define the contribution of surface energy as (in dimensional units)

$$E_S = \lim_{R \to \infty} \frac{1}{R} \int_{|x| < R} \frac{\sigma}{2} |\nabla h|^2 dx.$$
 (E1)

By writing $|\nabla h|^2 = \nabla \cdot (h \nabla h) - h \Delta h$ in (E1), where Δ denotes the Laplacian operator, and applying the divergence theorem to the first term, we obtain

$$E_S = \lim_{R \to \infty} \frac{1}{R} \left[\frac{\sigma}{2} \int_{|\mathbf{x}| = R} h \, \nabla h \cdot \mathbf{n} \, \mathrm{d}s - \int_{|\mathbf{x}| \le R} \frac{\sigma}{2} h \, \Delta h \, \mathrm{d}\mathbf{x} \right], \tag{E2}$$

where n is the outward-pointing unit vector to the circle |x| = R, and ds denotes line integration. Owing to the far-field decay of the wave field, we see that the boundary integral in (E2) vanishes in the limit $R \to \infty$, leaving

$$E_S = \lim_{R \to \infty} \frac{1}{R} \int_{|\mathbf{x}| \le R} -\frac{\sigma}{2} h \, \Delta h \, \mathrm{d}\mathbf{x}. \tag{E3}$$

Finally, we recall that the wave field is composed of monochromatic Bessel functions with wavenumber k_F . It follows that $\Delta h = -k_F^2 h$ for our wave model, which allows us to reduce (E3) to the simplified form

$$E_S = \lim_{R \to \infty} \frac{1}{R} \int_{|x| < R} \frac{\sigma k_F^2}{2} h^2(x, t) \, \mathrm{d}x, \tag{E4}$$

which is proportional to the contribution from the gravitational potential energy.

E.2. Wave intensity for orbital motion

To compute the wave intensity for a given droplet trajectory, we first introduce the polar coordinate system $x = r(\cos \theta, \sin \theta)$ and decompose the dimensionless wave field (see (4.4)) as

$$\hat{h}(x,t) = \sum_{n=-\infty}^{\infty} a_n(t) J_n(r) e^{in\theta}.$$
 (E5)

By substituting (E5) into (4.4) and applying Graf's addition theorem (Abramowitz & Stegun 1948), we find that each coefficient $a_n(t)$ is defined by the integral (Labousse *et al.* 2014)

$$a_n(t) = \int_{-\infty}^t J_n(r_p(s)) e^{-in\theta_p(s)} e^{-\mu(t-s)} ds,$$
 (E6)

where $x_p(t) = r_p(t) (\cos \theta_p(t), \sin \theta_p(t))$ is the droplet position. Finally, by substituting (E5) into (4.3), applying Parseval's theorem in the azimuthal direction, evaluating the

integral in the radial direction, and taking the limit $R \to \infty$, we obtain (Labousse *et al.* 2016*b*; Hubert *et al.* 2022)

$$\hat{E}(t) = \sum_{n = -\infty}^{\infty} |a_n(t)|^2.$$
 (E7)

We proceed to evaluate the wave intensity for the wave field accompanying a droplet orbiting the origin. By substituting $r_p(t) = r_0$ and $\theta_p(t) = \omega t$ into (E6) and evaluating the resultant integral, we deduce that

$$a_n(t) = \frac{J_n(r_0)e^{-in\omega t}}{\mu - in\omega}.$$
 (E8)

Upon substituting $a_n(t)$ into (E7), we thus deduce

$$\hat{E} = \sum_{n=-\infty}^{\infty} \frac{J_n^2(r_0)}{\mu^2 + n^2 \omega^2},$$
 (E9)

whereupon comparing this equation with (B3) determines the expression given in (4.5).

REFERENCES

ABRAMOWITZ, M. & STEGUN, I.A. 1948 Handbook of Mathematical Functions with Formulas, Graphs, and Mathematical Tables, vol. 55. US Government Printing Office.

Arbelaiz, J., Oza, A.U. & Bush, J.W.M. 2018 Promenading pairs of walking droplets: dynamics and stability. *Phys. Rev. Fluids* 3, 013604.

BACOT, V., PERRARD, S., LABOUSSE, M., COUDER, Y. & FORT, E. 2019 Multistable free states of an active particle from a coherent memory dynamics. *Phys. Rev. Lett.* **122**, 104303.

BAKKER, M. & TEMME, N.M. 1984 Sum rule for products of Bessel functions: comments on a paper by Newberger. J. Math. Phys. 25 (5), 1266–1267.

BENJAMIN, T.B. & URSELL, F. 1954 The stability of the plane free surface of a liquid in vertical periodic motion. *Proc. R. Soc. Lond.* A **225**, 505–515.

BLEISTEIN, N. & HANDELSMAN, R.A. 1975 Asymptotic Expansions of Integrals. Ardent Media.

BORGHESI, C., MOUKHTAR, J., LABOUSSE, M., EDDI, A., FORT, E. & COUDER, Y. 2014 Interaction of two walkers: wave-mediated energy and force. *Phys. Rev.* E **90**, 063017.

DE BROGLIE, L. 1926 Ondes et Mouvements. Gauthier-Villars.

DE BROGLIE, L. 1930 An Introduction to the Study of Wave Mechanics. Methuen & Co.

BUSH, J.W.M. 2015 Pilot-wave hydrodynamics. Annu. Rev. Fluid Mech. 47, 269-292.

BUSH, J.W.M. & OZA, A.U. 2020 Hydrodynamic quantum analogs. Rep. Prog. Phys. 84, 017001.

BUSH, J.W.M., OZA, A.U. & MOLÁČEK, J. 2014 The wave-induced added mass of walking droplets. J. Fluid Mech. 755, R7.

COUCHMAN, M.M.P. & BUSH, J.W.M. 2020 Free rings of bouncing droplets: stability and dynamics. J. Fluid Mech. 903, A49.

COUCHMAN, M.M.P., TURTON, S.E. & BUSH, J.W.M. 2019 Bouncing phase variations in pilot-wave hydrodynamics and the stability of droplet pairs. *J. Fluid Mech.* 871, 212–243.

COUDER, Y. & FORT, E. 2006 Single particle diffraction and interference at a macroscopic scale. Phys. Rev. Lett. 97, 154101.

COUDER, Y., FORT, E., GAUTIER, C.-H. & BOUDAOUD, A. 2005a From bouncing to floating: noncoalescence of drops on a fluid bath. Phys. Rev. Lett. 94, 177801.

COUDER, Y., PROTIÈRE, S., FORT, E. & BOUDAOUD, A. 2005b Walking and orbiting droplets. *Nature* 437, 208

CRISTEA-PLATON, T., SÁENZ, P.J. & BUSH, J.W.M. 2018 Walking droplets in a circular corral: quantisation and chaos. Chaos 28, 096116.

DELVES, L.M. & LYNESS, J.N. 1967 A numerical method for locating the zeros of an analytic function. *Math. Comput.* 21 (100), 543–560.

DUREY, M. 2018 Faraday wave-droplet dynamics: a hydrodynamic quantum analogue. PhD thesis, University of Bath.

- DUREY, M. & BUSH, J.W.M. 2021 Classical pilot-wave dynamics: the free particle. Chaos 31, 033136.
- DUREY, M. & MILEWSKI, P.A. 2017 Faraday wave-droplet dynamics: discrete-time analysis. *J. Fluid Mech.* **821**, 296–329.
- DUREY, M., MILEWSKI, P.A. & BUSH, J.W.M. 2018 Dynamics, emergent statistics and the mean-pilot-wave potential of walking droplets. *Chaos* 28, 096108.
- DUREY, M., MILEWSKI, P.A. & WANG, Z. 2020a Faraday pilot-wave dynamics in a circular corral. J. Fluid Mech. 891, A3.
- DUREY, M., TURTON, S.E. & BUSH, J.W.M. 2020b Speed oscillations in classical pilot-wave dynamics. *Proc. R. Soc.* A **476**, 20190884.
- EDDI, A., FORT, E., MOISY, F. & COUDER, Y. 2009 Unpredictable tunneling of a classical wave–particle association. *Phys. Rev. Lett.* **102**, 240401.
- EDDI, A., SULTAN, E., MOUKHTAR, J., FORT, E., ROSSI, M. & COUDER, Y. 2011 Information stored in Faraday waves: the origin of a path memory. *J. Fluid Mech.* **674**, 433–463.
- ELLEGAARD, C. & LEVINSEN, M.T. 2020 Interaction of wave-driven particles with slit structures. *Phys. Rev.* E **102**, 023115.
- FORT, E., EDDI, A., MOUKHTAR, J., BOUDAOUD, A. & COUDER, Y. 2010 Path-memory induced quantization of classical orbits. *Proc. Natl Acad. Sci.* 107 (41), 17515–17520.
- GALEANO-RIOS, C.A., COUCHMAN, M.M.P., CALDAIROU, P. & BUSH, J.W.M. 2018 Ratcheting droplet pairs. *Chaos* 28, 096112.
- GRADSHTEYN, I.S. & RYZHIK, I.M. 2014 Table of Integrals, Series, and Products. Academic Press.
- HARRIS, D.M. & BUSH, J.W.M. 2014 Drops walking in a rotating frame: from quantized orbits to multimodal statistics. *J. Fluid Mech.* **739**, 444–464.
- HARRIS, D.M., MOUKHTAR, J., FORT, E., COUDER, Y. & BUSH, J.W.M. 2013 Wavelike statistics from pilot-wave dynamics in a circular corral. *Phys. Rev.* E **88**, 011001.
- HUBERT, M., LABOUSSE, M., PERRARD, S., LABOUSSE, M., VANDEWALLE, N. & COUDER, Y. 2019 Tunable bimodal explorations of space from memory-driven deterministic dynamics. *Phys. Rev.* E 100, 032201.
- HUBERT, M., PERRARD, S., VANDEWALLE, N. & LABOUSSE, M. 2022 Overload wave-memory induces amnesia of a self-propelled particle. *Nat. Commun.* 13 (1), 4357.
- KURIANSKI, K.M., OZA, A.U. & BUSH, J.W.M. 2017 Simulations of pilot-wave dynamics in a simple harmonic potential. *Phys. Rev. Fluids* 2, 113602.
- LABOUSSE, M. 2014 Étude d'une dynamique à mémoire de chemin: une expérimentation théorique. PhD thesis, Université Pierre et Marie Curie UPMC Paris VI.
- LABOUSSE, M., OZA, A.U., PERRARD, S. & BUSH, J.W.M. 2016a Pilot-wave dynamics in a harmonic potential: quantization and stability of circular orbits. *Phys. Rev.* E **93**, 033122.
- LABOUSSE, M. & PERRARD, S. 2014 Non-Hamiltonian features of a classical pilot-wave dynamics. *Phys. Rev.* E **90**, 022913.
- LABOUSSE, M., PERRARD, S., COUDER, Y. & FORT, E. 2014 Build-up of macroscopic eigenstates in a memory-based constrained system. New J. Phys. 16, 113027.
- LABOUSSE, M., PERRARD, S., COUDER, Y. & FORT, E. 2016b Self-attraction into spinning eigenstates of a mobile wave source by its emission back-reaction. *Phys. Rev.* E **94**, 042224.
- MILES, J. & HENDERSON, D. 1990 Parametrically forced surface waves. Annu. Rev. Fluid Mech. 22, 143–165.
 MOLÁČEK, J. & BUSH, J.W.M. 2013a Droplets bouncing on a vibrating fluid bath. J. Fluid Mech. 727, 582–611.
- MOLÁČEK, J. & BUSH, J.W.M. 2013b Drops walking on a vibrating bath: towards a hydrodynamic pilot-wave theory. J. Fluid Mech. 727, 612–647.
- NEWBERGER, B.S. 1982 New sum rule for products of Bessel functions with application to plasma physics. J. Math. Phys. 23 (7), 1278–1281.
- OZA, A.U. 2014 A trajectory equation for walking droplets: hydrodynamic pilot-wave theory. PhD thesis, Massachusetts Institute of Technology.
- OZA, A.U., HARRIS, D.M., ROSALES, R.R. & BUSH, J.W.M. 2014a Pilot-wave dynamics in a rotating frame: on the emergence of orbital quantization. *J. Fluid Mech.* 744, 404–429.
- OZA, A.U., ROSALES, R.R. & BUSH, J.W.M. 2013 A trajectory equation for walking droplets: hydrodynamic pilot-wave theory. *J. Fluid Mech.* **737**, 552–570.
- OZA, A.U., ROSALES, R.R. & BUSH, J.W.M. 2018 Hydrodynamic spin states. Chaos 28, 096106.
- OZA, A.U., SIÉFERT, E., HARRIS, D.M., MOLÁČEK, J. & BUSH, J.W.M. 2017 Orbiting pairs of walking droplets: dynamics and stability. *Phys. Rev. Fluids* 2, 053601.
- OZA, A.U., WIND-WILLASSEN, Ø., HARRIS, D.M, ROSALES, R.R. & BUSH, J.W.M. 2014b Pilot-wave hydrodynamics in a rotating frame: exotic orbits. *Phys. Fluids* **26**, 082101.

N. Liu, M. Durey and J.W.M. Bush

- PERRARD, S., LABOUSSE, M., FORT, E. & COUDER, Y. 2014a Chaos driven by interfering memory. *Phys. Rev. Lett.* 113, 104101.
- PERRARD, S., LABOUSSE, M., MISKIN, M., FORT, E. & COUDER, Y. 2014b Self-organization into quantized eigenstates of a classical wave-driven particle. *Nat. Commun.* 5, 3219.
- PUCCI, G., HARRIS, D.M., FARIA, L.M. & BUSH, J.W.M. 2018 Walking droplets interacting with single and double slits. *J. Fluid Mech.* 835, 1136–1156.
- SÁENZ, P.J., CRISTEA-PLATON, T. & BUSH, J.W.M. 2018 Statistical projection effects in a hydrodynamic pilot-wave system. Nat. Phys. 14, 315–319.
- SÁENZ, P.J., CRISTEA-PLATON, T. & BUSH, J.W.M. 2020 A hydrodynamic analog of Friedel oscillations. Sci. Adv. 6 (20), eaay9234.
- SÁENZ, P.J., PUCCI, G., TURTON, S.E., GOUJON, A., ROSALES, R.R., DUNKEL, J. & BUSH, J.W.M. 2021 Emergent order in hydrodynamic spin lattices. *Nature* **596**, 58–62.
- TADRIST, L., GILET, T., SCHLAGHECK, P. & BUSH, J.W.M. 2020 Predictability in a hydrodynamic pilot-wave system: resolution of walker tunneling. *Phys. Rev.* E **102**, 013104.
- TADRIST, L., SHIM, J.-B., GILET, T. & SCHLAGHECK, P. 2018 Faraday instability and subthreshold Faraday waves: surface waves emitted by walkers. *J. Fluid Mech.* **848**, 906–945.
- TAMBASCO, L.D. & BUSH, J.W.M. 2018 Exploring orbital dynamics and trapping with a generalized pilot-wave framework. *Chaos* 28, 096115.
- THOMSON, S.J., DUREY, M. & ROSALES, R.R. 2020 Collective vibrations of a hydrodynamic active lattice. *Proc. R. Soc.* A **476**, 20200155.
- TURTON, S.E., COUCHMAN, M.M.P. & BUSH, J.W.M. 2018 A review of the theoretical modeling of walking droplets: towards a generalized pilot-wave framework. *Chaos* 28, 096111.